

Grey-box modeling and hypothesis testing of functional near-infrared spectroscopy-based cerebrovascular reactivity to anodal high-definition tDCS in healthy humans

Yashika Arora

Indian Institute of Technology Mandi

Pushpinder Walia

University at Buffalo, State University of New York

Mitsuhiro Hayashibe

Tohoku University

Makii Muthalib

University of Montpellier

Shubhajit Roy Chowdhury (✉ src@iitmandi.ac.in)

Indian Institute of Technology Mandi

Stephane Perrey

University of Montpellier

Anirban Dutta (✉ anirband@buffalo.edu)

University at Buffalo, State University of New York

Research Article

Keywords: Cerebral Blood Flow, Cerebrovascular Reactivity, Hemodynamics, Near-Infrared Spectroscopy, Neurovascular Coupling, Transcranial Electrical Stimulation

Posted Date: February 16th, 2021

DOI: <https://doi.org/10.21203/rs.3.rs-83907/v3>

License:  This work is licensed under a Creative Commons Attribution 4.0 International License.

[Read Full License](#)

Version of Record: A version of this preprint was published at PLOS Computational Biology on October 6th, 2021. See the published version at <https://doi.org/10.1371/journal.pcbi.1009386>.

Abstract

Transcranial direct current stimulation (tDCS) has been shown to evoke hemodynamics response; however, the mechanisms have not been investigated systematically using systems biology approaches. We postulate that such a mechanistic understanding of the hemodynamics response, called cerebrovascular reactivity (CVR) to tDCS, can facilitate adequate delivery of the tDCS current density to the neurovascular tissue in cerebrovascular diseases. Our study presents a systems biology approach to evaluate CVR during high-definition (HD) tDCS using a physiologically constrained grey-box linear model. Our grey-box linear model was developed for the multi-compartmental neurovascular unit consisting of the vascular smooth muscle, perivascular space, synaptic space, and astrocyte glial cell. The physiologically detailed model generated vessel oscillations in the frequency range of 0.05–0.2 Hz driven mainly by non-linear calcium dynamics. Then, model linearization was performed to develop a grey-box linear model for evaluating the acute effects during the first 150 seconds of anodal HD-tDCS in eleven healthy humans using functional near-infrared spectroscopy (fNIRS) based measure of blood volume. The grey-box linear model was fitted to the total hemoglobin concentration (tHb) changes with optodes in the vicinity of 4x1 HD-tDCS electrodes. We found that the grey-box model pathway from perivascular potassium to the vessel circumference (Pathway 3) presented the best fit to fNIRS tHb time series with the least mean square error (MSE, median < 2.5%). Then, minimal realization transfer function with reduced-order approximations of the grey-box model pathways was fitted to the average tHb time series. Pathway 3, with nine poles and two zeros (all free parameters), provided the best Chi-Square Goodness of Fit of 0.0078. Therefore, our study provided a sound systems biology approach to investigate the hemodynamic response to tDCS that needs further investigation in health, aging, and disease. Future studies can leverage transcranial alternating current stimulation for frequency-dependent physiological entrainment of relevant pathways, e.g., oscillations driven by nonlinear calcium dynamics, that can provide additional insights based on our grey-box modeling approach.

Introduction

Cerebral blood flow (CBF) regulation is crucial for normal brain activity where hypoperfusion has been associated with cerebrovascular diseases, including cognitive impairment in various cross-sectional studies¹. Cerebrovascular disease refers to conditions that have an effect on blood vessels and blood supply to the brain². Since vascular factors are an important contributor to cerebrovascular disease, including a role in mild cognitive impairment and dementia³, that is predicted to increase to 152 million by 2050⁴; therefore, therapeutic measures for the cerebrovascular disease are crucial. Transcranial electrical stimulation (tES), particularly transcranial direct current (tDCS), has been shown to be a promising therapeutic method that can evoke regional CBF⁵, which may be able to ameliorate hypoperfusion and the related cognitive impairments. Here, CBF is regulated primarily by three mechanisms, cerebral autoregulation that maintains the CBF under changes in systemic blood pressure; cerebral vasoreactivity that is the response to the arterial CO₂ partial pressure changes; and neurovascular coupling that is the response to the neuronal activity. However, the physiological

mechanisms of tDCS evoked CBF response is unknown^{6,7}. A recent study⁸ showed that the spatial distribution of CBF changes correlated with the tDCS-induced electric field distribution (< 1 V/m) computed using finite element modeling. CBF changes can also be evoked rapidly (< 100 ms) with transcranial alternating current stimulation at 10–20 Hz; however, at higher electric field strengths (5–20 V/m)⁹. Since neurovascular coupling related hemodynamic response should start about 600 ms following the stimulus based on an experimental study by Devor et al.¹⁰; therefore, such rapid changes in the CBF is postulated to indicate the direct effect of the electric field on the vascular neural network^{6,7,11} (e.g., perivascular nerves, neuronal nitric oxide expressing interneuron¹²). The proximal pial arteries and the descending arteries have the fastest onset time followed by the capillaries (spatiotemporal characteristics of pial, penetrating, and micro-vessels are summarized in Schmid et al.¹³), where direct neurocapillary modulation by tDCS may also be possible¹⁴. Consequently, the resultant spatiotemporal dynamics of the vascular response to electrical stimulation can be quite complex due to the interdependence of the nested spatiotemporal dynamics of the pial arteries, descending arteries, and the capillaries. Therefore, individual hemodynamic effects of the tDCS current density via various neurovascular pathways need to be investigated using mechanistic model-based hypothesis testing where CBF responses can be site-specific and subject-specific¹⁵.

The neuromodulatory consequences of tDCS are understood to be generated due to the induced electric field (and current density) in the cortex by applying a weak direct current through scalp electrodes, causing cortical excitability changes¹⁶. It is evident from the neurophysiological studies that the induced electric field can change neuronal excitability with current intensities ranging from 0.7 to 2.0 mA over 9–20 minute sessions¹⁷. The current applied by surface electrodes in tDCS is shunted through the scalp, and cerebrospinal fluid (CSF). Only a fraction of the current reaches the cortex, producing a weak electric field (~ 0.3 V/m per 1mA of applied current)^{18,19} that can subthreshold polarize the neurons. However, persistent (> 9 min) weak electric field can lead to neuroplastic changes and excitability after-effects, postulated to be driven by persistent calcium flux, which in turn can affect cortical excitability²⁰, alter the firing rate of neurons^{21,22}, and modify spatiotemporal brain networks related to information transfer in the brain^{18,23}. So, a majority of research on tDCS has focused on cortical neuronal after-effects following long duration (> 9 min) weak electric field²⁴ stimulation; however, investigation of the immediate effects of the electric field on all neurovascular targets in the cortical tissue may accord to better understanding of the vascular neural network¹¹ mechanisms to hemodynamic response. For example, Guhathakurta and Dutta²⁵ postulated based on finite element modeling that the pial arteries (and arterioles) contain perivascular nerves within their adventitial layer that can be strongly affected by tDCS-induced electric field since the magnitude of the tDCS current density in the cerebrospinal fluid (CSF) that surrounds pial vessels can be much higher than that in the brain parenchyma – details in the supplementary materials (section H: Electric Field in brain tissues, see Supplementary Figure S4). Autonomic nerve fibers including noradrenergic perivascular axons, richly innervate the cerebral vessels within their adventitial layer, especially the larger arteries including pial vessels, and tDCS electric field can affect the limits of vasomotor control²⁶ and the autoregulation plateau²⁷. Autoregulation is important since pial arteries start

the pressure-driven blood pathway to the cortex and have a robust network topology that guarantees a constant blood supply (reviewed in Schmid et al.¹³). Also, the pial arterial network structure on the cortical surface is comparable to that of a honeycomb²⁸ that can cause distortion of the current flow from the CSF into the gray matter (GM) due to the large differences in the conductivity²⁹ of the CSF, blood vessels¹⁴, and GM. Such current flow distortion around the blood vessels¹⁴ may be responsible for the vascular neural network¹¹ stimulation (that can affect their excitability⁷) and distort the electric field in the gray matter that needs further investigation.

In this study, we considered mechanistic model-based hypothesis testing of the coupling mechanisms where neuronal and vascular functions are closely interconnected through neurovascular mechanisms, as evident from studies using functional magnetic resonance imaging (fMRI), positron emission tomography (PET), and, more recently, functional near-infrared spectroscopy (fNIRS). fNIRS provides a portable optical imaging technology that can be conducted in conjunction with transcranial electrical stimulation without interference. Therefore, combining tDCS with fNIRS is feasible to capture variable neurovascular and neurometabolic effects; however, physiologically guided mechanistic models are necessary for hypothesis testing in systems biology. From an anatomical perspective, an integrated system of neurons, astrocytes, and vascular cells form a neurovascular unit (NVU) that facilitates brain homeostasis and links neuronal, metabolic, and vascular activities at cellular level^{30,31}. So, tDCS can directly affect the excitability of the cortical neurons and can also have an indirect effect via vascular neural network¹¹ and neuronal nitric oxide (nNOS) expressing interneuron¹² or modulatory effects on non-neuronal cells^{32,33}. Mathematical models of NVU are well published in fMRI, which can span from completely phenomenological to detailed mechanistic models (described in the Methods section). Data-driven black-box systems approaches provide a correlate of neural and hemodynamic response at an abstract level under the assumption of neurovascular coupling at the cellular level; however, such black-box systems approaches do not aim to explicitly capture the underlying cellular mechanisms of action. Considering the evidence of modulatory consequences of tDCS on blood vessels that can be via neuronal and non-neuronal cells, a deeper understanding of the signaling pathways inside the NVU is essential for a mechanistic understanding. Such a mechanistic understanding of the signaling pathways inside the NVU is necessary for systematic investigation of tDCS-induced electric field effects on the hemodynamics in health, aging, and disease²⁶ that we have called cerebrovascular reactivity (CVR) to tDCS³⁴.

In our grey-box model, CVR was based on a change in the blood circumference (and blood volume) in response to tDCS. In healthy tissue, CVR is a compensatory mechanism where blood vessels dilate in immediate response to the vasodilatory stimulus to regulate the resistance to the flow, modifying the cerebral perfusion³⁵. We postulate that the immediate hemodynamic response⁹ based on CVR to short-duration tDCS can provide a marker of blood vessels' capacity to dilate that can be hampered in various cerebrovascular diseases^{36,37}. However, longer duration (> 9 min) tDCS will induce neuroplastic changes²⁴ where non-linear bidirectional neurovascular interactions³⁸ can make the mechanistic models

too complex for fNIRS data fitting and hypothesis testing. Therefore, the current study investigated the initial CVR to tDCS by grey-box linear modeling of the intimate relationship between neuronal activity and hemodynamic response that involved the signaling pathways across the lumped model of the NVU compartments. Although finite element modeling has indicated neurocapillary modulation by tDCS¹⁴ through the interaction of the electric field with the NVU; however, such detailed finite element modeling becomes challenging in predictive modeling due to folded cortical structures and complex vascular network, therefore, detailed finite element modeling without model tuning to fit individual functional data can produce unpredictable and variable results across subjects³⁹⁻⁴¹.

In this mathematical modeling and hypothesis testing paper, our systems biology investigation is based on the dynamics within the four compartments of the NVU: synaptic space, intracellular astrocyte space, perivascular space, and intracellular space of the arteriolar smooth muscle cell (SMC). We analyzed the pilot data from healthy participants from our prior work⁴² to evaluate the role of various signaling pathways within NVU using a grey-box linear systems identification approach. In a classical neurovascular coupling response, the initial phase includes an increase in deoxy-hemoglobin concentration (deoxy-Hb) and a decrease in oxy-hemoglobin concentration (oxy-Hb) that precede an overall rise in blood volume^{10,43}. Here, the indirect "metabolic hypothesis," states that an increase in neuronal synaptic activity causes additional energy and oxygen demand (i.e., an increase in deoxy-Hb and decrease in oxy-Hb), causing various vasodilation agents to send signals to cerebral vasculature for vasodilation, resulting in an increase in regional CBF and oxy-Hb concentration. This metabolic hypothesis can also explain the initial dip in oxy-Hb concentration in the period immediately following tDCS before reaching peak levels, as observed in our previous study on ischemic brain^{42,44}. In healthy tissue, a rapid and large increase in oxy-Hb may be explained through direct "neurogenic hypothesis," whereby the direct modulation of neuropeptides and neurotransmitters by tDCS causes a discharge of various vasoactive agents such as NO for vasodilation and an increase in oxy-Hb⁴⁵. Such a "neurogenic hypothesis" can also be applied to the perivascular nerves²⁶ and nNOS expressing interneuron, e.g., around the pial arteries and arterioles²⁵ have a compounding dilatory effect to the increase in the blood volume (and oxy-Hb). Therefore, the current study considered total hemoglobin (tHb) changes (related to blood volume changes⁴⁶), obtained by adding oxy-Hb and deoxy-Hb changes, during tDCS to account for the vessel volume changes to fit in our mathematical model. Here, tHb change was considered as a better measure of the change in the regional cerebral blood volume⁴⁶ compared to oxy-Hb or deoxy-Hb content taken individually. The signaling pathways modulating vascular response to the electric field in the perivascular space, astrocytes, and direct vascular SMCs were evaluated and compared using grey-box linear systems' transfer function analysis in eleven healthy participants from our prior experimental studies^{42,44}. In our previous works, Muthalib et al.⁴⁴ established the focality of the hemodynamic response where they found a more significant increase in oxy-Hb "within" than "outside" the spatial extent of the 4 × 1 high-definition (HD)-tDCS electrode as a hemodynamic correlate of the electrical field distribution. In the current study, we used that experimental data^{42,44} in conjunction with our novel grey-box linear model to investigate tHb as the hemodynamic correlate of the current density effects "within"

the spatial extent of the 4×1 HD-tDCS electrode. Here, the increase in the blood volume during HD-tDCS was considered to be caused by a mix of metabolic and neurogenic hypotheses.

Results

(A) fNIRS-tHb response during HD-tDCS (experimental data):

Figure 1 shows the change in the normalized tHb obtained during anodal HD-tDCS stimulation from fNIRS channels around the 4×1 HD-tDCS anode (montage shown in Fig. 6) and from the contralateral non-stimulated sensorimotor cortex. In most of the participants, the time course of changes in tHb in the region within the boundary of the HD-tDCS montage showed a steep initial increase compared to the contralateral non-stimulated sensorimotor area that showed a decrease in some participants, which may be related to inter-hemispheric inhibition.

(B) Physiologically detailed model response:

A physiologically detailed neurovascular coupling model was developed from published literature^{38,47-49}, as described in the Methods section (differential equations and model parameters (see Supplementary Table S1) in the supplementary materials, section A: Model Equations for Neurovascular Compartmental Dynamics). The four simulated pathways (see supplementary materials, section B: Pathways Equations in the supplementary materials) are shown in Fig. 2; 1) tDCS modulating vessel response through synaptic potassium pathway, 2) tDCS modulating vessel response through the astrocytic pathway, 3) tDCS modulating vessel response through perivascular potassium pathway, and 4) tDCS modulating vessel response through voltage-gated ion current channels on the SMC pathway. Figure 2(A) shows the HD-tDCS input, and Fig. 2(B) shows the simulated model output of the physiologically detailed model where the model output is blood vessel circumference, x , to the input trapezoidal current waveform. Here, the 2mA tDCS waveform, shown in Fig. 2(A), generated a vasoactive signal in the four pathways at the compartments of the lumped model of the NVU. While simulating the physiologically detailed neurovascular coupling model, the vasoactive signals for the pathways were represented as a first-order transfer function of the input current waveform, i.e., approximated by a first-order filter (with 20 ms time constant). For Pathway 1, the effect of tDCS current density on the synaptic potassium concentration was considered, which drove the neurovascular dynamics leading to the blood vessel (circumference) response. The effect of tDCS current density on astrocytic membrane potential, perivascular potassium currents, and SMCs leading to the vessel (circumference) response were modeled by Pathways 2, 3, and 4, respectively (see supplementary materials, section B: Pathways Equations in the supplementary materials). Figure 2(B) shows that physiologically detailed neurovascular coupling pathways generated low-frequency oscillations in the frequency range of 0.05–0.2 Hz, driven by nonlinear calcium dynamics in various compartments, during the time course of the vessel response.

(C) Physiologically detailed model linearization for grey-box analysis of experimental data:

For the grey-box analysis of the fNIRS tHb (normalized) as output to the input tDCS current waveform (normalized), model reduction of the four pathways from the physiologically detailed model was performed using Simulink's linear analysis tool (MathWorks, Inc., USA). This tool allows the linearization of complex nonlinear models at different operating points. We assumed that the subthreshold tDCS current density perturbation to the different pathways of the lumped NVU model would operate close to the resting-state baseline conditions at all the compartments, especially during the initial period (< 3 min) after tDCS onset until neuroplastic changes occur (neuroplastic after-effects > 3 min of tDCS¹⁶). Therefore, the physiologically detailed model linearization was performed at the initial conditions from published literature^{38,47-49} as described in the Methods section. Here, the linearization step approximated the system of nonlinear differential equations around the initial resting-state conditions. The linear model presented the neurovascular system as a set of input, internal states (compartment variables), and output as transfer functions, which depicted the relationship between input current waveform (normalized) and the output tHb (normalized) hemodynamic response. The linearized model was then used for grey-box linear modeling with identifiable parameters ('idgrey' in MATLAB, MathWorks, Inc., USA). The linearized grey-box model did not capture low-frequency oscillations in the frequency range of 0.05–0.2 Hz so we limited the fNIRS tHb data within the lower frequency band (0.01–0.05Hz) of the nested effects of neurovascular coupling, vasomotor control, and autoregulation²⁷ during initial 150sec (30sec ramp-up + 120sec steady-state) of tDCS.

(D) Linear grey-box model analysis using experimental fNIRS-tHb data:

The System Identification Toolbox (MathWorks, Inc., USA) was used to grey-box model the time-domain tDCS input (normalized current waveform) and fNIRS output (normalized tHb) data from eleven healthy participants. The input time-series was a trapezoidal waveform, and output time-series were normalized values of the average fNIRS-tHb changes in the vicinity of the 4 x 1 HD-tDCS electrodes at the sensorimotor cortex during the initial 150 secs (30sec ramp-up and 2 min steady-state so < 3 min) of HD-tDCS. We also fitted the grey-box linear model to the average fNIRS-tHb changes at the non-stimulated (montage is shown in Fig. 6) contralateral sensorimotor cortex (details in the Methods section). The grey-box linear model with identifiable parameters obtained after model linearization of the physiologically detailed non-linear model was taken as the initial system to fit the experimental fNIRS-tHb data from 0–150 sec during HD-tDCS from each participant. Initial 150 sec (ramp-up period of 30 sec + 2 minutes) was assumed to be unaffected by neuroplastic after-effects (mainly calcium-dependent) of tDCS¹⁶. Figure 3 shows the simulated grey-box linear model output, i.e., normalized fNIRS-tHb (assumed proportional to vessel volume change) of the four pathways for each of the 11 participants, P1-P11 (individual grey-box transfer functions are tabulated in the Supplementary Table S3 in the supplementary materials). Figures 3 (A1) – (A4) show the four simulated pathways at the HD-tDCS stimulated sensorimotor cortex

while Figs. 3 (B1) – (B4) show the four simulated pathways at the contralateral non-stimulated sensorimotor cortex for each participant – see electric field modeling in Fig. 7 and contralateral optodes, C2-FC4, C6-FC4, C2-CP4, and C6-CP4, in Fig. 6. Table 1A shows the mean square error (MSE) for each participant for the grey-box linear model that fits the HD-tDCS stimulated sensorimotor cortex. Table 1B shows the MSE for each participant for the model fits at the contralateral non-stimulated sensorimotor cortex. Here, Pathway 3, from the perivascular potassium to vessel circumference, presented the least MSE (median < 2.5%) across all participants, followed by Pathway 1, as shown in Fig. 4. Pathway 1 gave < 6% median MSE across all participants for the grey-box linear model fits at the contralateral non-stimulated sensorimotor cortex, which is postulated to be related to inter-hemispheric inhibition. For MSE comparison with long-term tDCS effects, grey-box modeling of the complete 10 min of tHb data at the HD-tDCS stimulated sensorimotor cortex was performed (see Supplementary Figure S1 in the supplementary materials) where Pathway 3 resulted in the lowest MSE (< 0.5% median). The MSE results had a similar distribution across four pathways, as shown by comparing Supplementary Figure S2 (in the supplementary materials) and Fig. 4(A). Residuals checks were performed based on the autocorrelation curves of the residuals and the cross-correlation curves between input and the residuals that were better for 150sec fits – see supplementary materials (Supplementary Figure S3, section G: Residual checks)

Table 1A. Mean-square error (MSE) for the grey-box model analysis using the initial 150sec of fNIRS-tHb data from each participant's stimulated sensorimotor cortex for the four model pathways. *participants have greater than -0.5 correlation coefficient between oxy-Hb & deoxy-Hb - indicating low contrast-to-noise-ratio⁵⁰.

Participant#	Pathway 1 (Synaptic Potassium → vessel circumference)	Pathway 2 (Astrocytic membrane potential → vessel circumference)	Pathway 3 (Perivascular Potassium → vessel circumference)	Pathway 4 (Voltage-gated ion channel on SMC → vessel circumference)
P1	0.07055	0.2295	0.0422	0.09602
P2	0.02375	0.05435	0.001509	0.03862
P3*	0.02323	0.05801	0.02595	0.05892
P4*	0.01579	0.08174	0.05264	0.01266
P5	0.006357	0.01926	0.00382	0.02457
P6	0.02273	0.03176	0.01555	0.01968
P7	0.06432	0.1134	0.06047	0.1084
P8	0.02715	0.02585	0.03409	0.03307
P9	0.02488	0.00156	0.004376	0.001343
P10*	0.009925	0.05779	0.01008	0.02365
P11	0.03855	0.04509	0.01875	0.05301
Mean	0.029748	0.065301	0.024494	0.042722

Table 1B. Mean-square error (MSE) for the grey-box model analysis using the initial 150sec of fNIRS-tHb data from each participant's non-stimulated contralateral sensorimotor area the four model pathways. *participants have greater than -0.5 correlation coefficient between oxy-Hb & deoxy-Hb at the stimulated sensorimotor cortex - indicating low contrast-to-noise-ratio⁵⁰.

Participant#	Pathway 1 (Synaptic Potassium → vessel circumference)	Pathway 2 (Astrocytic membrane potential → vessel circumference)	Pathway 3 (Perivascular Potassium → vessel circumference)	Pathway 4 (Voltage-gated ion channel on SMC → vessel circumference)
P1	0.1229	0.2741	0.162	0.1898
P2	0.04355	0.06401	0.07775	0.01848
P3*	0.0901	0.347	0.08637	0.09435
P4*	0.04326	0.217	0.2944	0.1237
P5	0.0245	0.1864	0.2464	0.02318
P6	0.0593	0.02059	0.1225	0.01465
P7	0.07142	0.0689	0.195	0.0683
P8	0.02989	0.05707	0.02207	0.03159
P9	0.04824	0.09063	0.004094	0.01612
P10*	0.01748	0.01321	0.01051	0.02899
P11	0.02444	0.02422	0.07726	0.03184
Mean	0.05228	0.123921	0.118032	0.058273

The grey-box model simulated output of all the four pathways demonstrated an initial dip in the tHb concentration (related to the vessel circumference in the physiologically detailed model) which was based on the experimental data (see Supplementary materials, section D: Oxy and Deoxy-Hemoglobin Changes at the Stimulated Region). The parameterized grey-box linear model derived from a detailed physiological model had many states (see Supplementary Table S3 in the supplementary materials) where the numerator and denominator polynomial roots are known as model zeros and model poles, respectively. The model poles and zeros are useful in evaluating a system as their values govern the system's stability and performance. For a stable system, all the model poles must have negative real values. The model zeros are related to the response speed for a given system that captured the initial dip in the tHb concentration with positive zero in the right-half-plane (positive real axis for parameters of transfer function). Specifically, this model zero in the right-half-plane slowed the time response and resulted in the undershoot response. A positive zero adds to the phase lag in a system wherein the response initially becomes negative or changes direction to that of the required direction before converging in the desired steady state. However, such states can have relatively small energy contributions to system dynamics; so, a minimal realization transfer function with reduced-order approximations (see the Methods section for details) for the four pathways can provide better insights into the linear time-invariant system.

(E) Reduced dimension grey-box linear model analysis:

Table 2 shows the reduced-order approximations of high-order grey-box linear models (see Supplementary Table S3 in the supplementary materials). All the pathways have an excess of model poles over the number of zeros; therefore, the frequency response magnitude will tend to zero with an increasing frequency. However, the numbers of model zeros are different in the four pathways, where the positive real zeros are most likely approximating the system's time delay. All four pathways have complex

conjugate poles (from $s^2 + 9.804s + 95.24$ terms) in the stable region. Figure 5(A) shows the normalized impulse response function of the reduced dimension transfer function for the four pathways where Pathway 1 (TF1(s)) had 11 poles, and 3 zeros, Pathway 2 (TF2(s)) had 10 poles, and 3 zeros, Pathway 3 (TF3(s)) had 8 poles and 2 zeros. Pathway 4 (TF14(s)) had 6 poles and 1 zero as tabulated in Table 2. Here, none of the reduced dimension transfer functions had an initial dip. This provided a qualitative analysis for CVR where Pathway 4 had the fastest response (peaked at 0.4 sec), and Pathway 1 had the slowest response (peaked at 5 sec). Pathway 1, acting via the synaptic potassium, resulted in the stereotypical time-to-peak⁵¹ in the hemodynamic response function of about 5 seconds after stimulus onset⁵². After cascading with the first-order transfer function for tDCS's vasoactive effects (see Eq. 1), the four pathways' minimal realization transfer functions were found from the average tHb time series across participants, as shown in the Fig. 5(B). Fitting of the "smallest" Pathway 4 model, TF4, with 7 poles and 1 zero (all free parameters) provided an MSE of 0.0031 and Chi-Square Goodness of Fit of 0.0104. Then, Pathway 3 model, TF3, with 9 poles and 2 zeros (all free parameters) provided an MSE of 0.0025 and Chi-Square Goodness of Fit of 0.0078. Then, the "larger" Pathway 2 model, TF2, with 11 poles and 3 zeros (all free parameters) provided an MSE of 0.0025 and Chi-Square Goodness of Fit of 0.0085. The "largest" Pathway 1 model, TF1, with 12 poles and 3 zeros (all free parameters) provided an MSE of 0.0264 and Chi-Square Goodness of Fit of 0.0647. Here, more parameters in the "larger" models reduced the degrees of freedom, so worsened the Chi-Square Goodness of Fit even with similar MSE, e.g., TF2 and TF3. Therefore, TF3 for Pathway 3 provided the best fit for the HD-tDCS-induced tHb changes within 0.01 and 0.05 Hz.

Table 2. Minimal realization transfer functions were obtained through Model Reducer (MATLAB, MathWorks, Inc., USA) for four model pathways from the detailed physiological model for the neurovascular unit compartment model.

Pathway transfer functions (TF)	Transfer functions from the compartmental neurovascular coupling model that were used for the initial parameterization of the four pathways	Parameterization
TF1. Synaptic Potassium → vessel circumference	$TF1(s) = \frac{1}{(s + 0.4)} TF2(s)$	11 poles, 3 zeros
TF2. Astrocytic membrane potential → vessel circumference	$TF2(s) = \frac{(s + 46.5)}{(s + 1.966)(s + 15.08)} TF3(s)$	10 poles, 3 zeros
TF3. Perivascular Potassium → vessel circumference	$TF3(s) = \frac{(s + 2.371e07)}{(s + 2.974e04)(s + 1)} TF4(s)$	8 poles, 2 zeros
TF4. Voltage gated ion channel on SMC → vessel circumference	$TF4(s) = \frac{(s + 2.962)}{(s + 9.594e06)(s + 20.69)(s + 3.3)(s + 0.2446)(s^2 + 9.804s + 95.24)}$	6 poles, 1 zero

Discussion

We performed a grey-box linear systems analysis of the fNIRS-based CVR measure (change in tHb) to anodal HD-tDCS in healthy humans. The hemodynamic response is crucial for dosing tDCS due to its role in action⁵³, which can lead to inter- and intra- subject variability in neuronal responses^{40,54}. Furthermore, tDCS can be a promising method to evoke regional CBF⁵ to ameliorate hypoperfusion in cerebrovascular diseases, including facilitating cognitive rehabilitation. The hemodynamic response to tDCS current density in the brain can be captured based on the tHb changes using our parameterized grey-box linear model. In the hemodynamic response, low-frequency oscillations can have frequencies between 0.01 and 0.2 Hz, where the top of that range is related to the conventional hemodynamic response function of 5 seconds – TF1(s) in Fig. 5. Lower frequency oscillations < 0.1Hz are related to vasomotor and myogenic activity in the terminal arteriole and micro-vessels²⁷. The current study investigated very low-frequency oscillations between 0.01 and 0.05 Hz that can originate from arterioles under neurogenic innervation^{27,26}. Our physiologically detailed model captured the related non-linear calcium dynamics that is of significance since the effect of tDCS on coupling between the neuronal and hemodynamic low frequency oscillations has been shown in our prior work⁴² that may represent tDCS effects on the cerebral astrocytes. Guhathakurta and Dutta²⁵ have postulated that tDCS electric field spread in the highly conductive CSF directly affects the pial arteries and arterioles that contain perivascular nerves within their adventitial layer. Since pial arteries start the pressure-driven blood pathway to the cortex (reviewed in Schmid et al.¹³) so direct electric field effects on the volume of pial arteries can lead to an

initial dip in the blood volume (and tHb) in the capillary bed that can be seen in few healthy subjects in Fig. 1A. Here, tDCS effects on the vascular neural network^{6,7,11} under “neurogenic hypothesis” is in contrast to the “metabolic hypothesis” that causes initial dip in oxy-Hb where vasoactive signals are generated around the capillaries that may be transmitted upstream to the penetrating artery and pial artery (see Fig. 7C) if the vasoactive signal intensity is large enough.

In the current study, fNIRS data consisted of changes in tHb at the ipsilateral (to HD-tDCS) and the contralateral sensorimotor cortex, where the biological criteria²⁶ were formulated in the frequency band of 0.01–0.05 Hz⁵⁵. So, tHb time series data were down-sampled to 0.1Hz to study the slow transient response during HD-tDCS. We applied a system identification approach using a physiologically constrained linear model to capture the fNIRS-based CVR to anodal HD-tDCS in healthy humans where the pathway from perivascular potassium to vessel circumference (i.e., Pathway 3) presented the lowest MSE (median < 2.5%), as shown in Fig. 4. Pathway 3 also gave the lowest MSE (median < 0.5%) when fitted to the whole 10 min of tHb time series during HD-tDCS (see Supplementary Table S4 and Supplementary Figure S2 in the supplementary materials). Therefore, the primary mechanism of action for the HD-tDCS-induced CVR between 0.01 and 0.05 Hz is postulated to be perivascular potassium that can be a significant determinant of the local pial vessel diameter⁵⁶. Figure 10 shows all the pathways contributing to HD-tDCS-induced CVR depending on the vessel circumferencesensitivity to those pathways. Also, pathway response time will be different, e.g., tDCS-induced changes in the synaptic potassium (i.e., Pathway 1) had the slowest effect on vessel circumference. Recent studies showed that tDCS-induced alterations in cerebral CBF could only partially be related to the cortical excitability changes⁸. Therefore, our mechanistic investigation of the vascular response to tDCS using a physiologically detailed model (differential equations in the supplementary materials, section A: Model Equations for Neurovascular Compartmental Dynamics) of the four pathways, namely, via synaptic space, astrocytic space, perivascular space, and smooth muscle cell space (depicted in Figs. 9 and 10) provided novel evidence supporting the postulated role of perivascular potassium in CVR to tDCS. Pathway 1 considered modulation of synaptic mediators by tDCS current density, which then mediates the vessel circumference's effect via perivascular and astrocyte compartments through nested neurovascular dynamics. This is based on conventional neurovascular coupling mechanism under the effect of tDCS current density on the neurons, where neuronal activity drives the hemodynamic response. Pathway 2 considered the change in the membrane potential of the astrocytic compartment due to tDCS current density, which then drives the vascular response (vessel circumference). Pathway 3 considered modulation of the potassium currents in the perivascular space by tDCS current density. Pathway 4 considered the direct influence of tDCS current density on the vasculature's smooth muscle cells leading to the vascular response (vessel circumference). Pathway 4 was based on prior evidence that the voltage-gated potassium channels on the SMC can respond to the electric field^{57,58}, especially those in the pial vasculature. In our proposed model for Pathway 4, SMC's membrane potential was modulated by the tDCS current density that modulated the voltage-gated potassium channel currents. In this study, we found the potassium currents, either in the synaptic compartment (Pathway 1) or in the perivascular compartment (Pathway 3), as the primary vasoactive signal related to CVR between 0.01 and 0.05 Hz.

The vasoactive signal modulation by tDCS current density was represented mathematically as a first-order filter as cascaded transfer function – see Fig. 10. Here, after the minimization of the cost to find the optimal parameters, the cost needs to be evaluated based on Chi-Square Goodness-of-Fit that determines the quality of fit⁵⁹ for such nested models. Table 2 shows the reduced dimension transfer functions for the four model pathways. Here, reduced dimension grey-box linear model for the Pathway 3 with 9 poles and 2 zeros (all free parameters) provided the best Chi-Square Goodness-of-Fit of 0.0078.

In this study, our goal was to investigate the role of various neuronal and non-neuronal pathways leading to the CVR to tDCS, as demonstrated experimentally by our prior works^{42,60,61}, through an objective physiologically constrained grey-box model that is summarized by a block diagram in Fig. 10. The physiologically detailed model was primarily derived from Witthoft and Karniadakis³⁸. The first model pathway considered the effect of tDCS on the synaptic space's vasoactive agent (potassium ions) where the linear analysis at the model's initial condition was represented by seventeen states, i.e., differential equations (details in supplementary materials, section A: Model Equations for Neurovascular Compartmental Dynamics). The transfer function order denotes the number of model poles where the reduced dimension grey-box model for the first pathway was represented by a twelfth order system that included a first-order linear filter for the tDCS's vasoactive effects – see Table 2. The reduced dimension grey-box model for the astrocytic-driven (Pathway 2) and the perivascular potassium-driven (Pathway 3) pathways were represented by eleventh and ninth order systems, respectively. For Pathway 4, the input path considered the influence of tDCS current density on SMC gated ion channel current, and the reduced dimension grey-box model for this pathway was represented as a seventh order system. The impulse response function of the Pathway 1 defining conventional hemodynamic response function peaked around 5 sec (see Fig. 5(A)) that was comparable to known hemodynamic responses⁶². This provided insights into the temporal dynamics where the vessel response through an astrocytic pathway or perivascular potassium pathway peaked around 2 sec found comparable to known capillary responses¹³. Our study attempted to identify the role of various neuronal and non-neuronal pathways using a reduced dimension lumped grey-box model of NVU based on the vascular response (using tHb) to anodal HD-tDCS in healthy humans. However, the linearized physiologically detailed model of the four pathways could not investigate the effects of the current density on low-frequency (0.05–0.2 Hz) oscillations driven primarily by the nonlinear calcium dynamics. In this study, the data was down-sampled to 0.1 Hz that removed the spontaneous rhythmic nonlinear calcium dynamics in the frequency range of 0.05–0.2 Hz⁶³, including the ~0.1 Hz hemodynamic oscillations in the fNIRS time series⁴². Here, ~0.1 Hz hemodynamic oscillations can be related to the synchronization of the intermittent release of calcium within vascular SMC⁶³ that was modeled in the physiologically detailed model, as shown by Fig. 2(B) (also see the equations 48–49 in the supplementary materials, section A: Model Equations for Neurovascular Compartmental Dynamics). Our prior works have found a significant cross-correlation between log (base-10) transformed electroencephalogram (EEG) band-power (0.5-11.25Hz) and fNIRS oxy-Hb signal in that low frequency (≤ 0.1 Hz) range⁴². Investigation of ~0.1 Hz oscillatory vessel response vis-à-vis neuronal response (EEG) to tDCS will require a parameterized coupled oscillator model. Here, the relation of the

~0.1 Hz oscillatory vessel response vis-à-vis neuronal response may be related to the cortical excitability changes to anodal tDCS⁶⁰ due to the involvement of calcium dynamics that needs future investigation using transcranial alternating current stimulation (tACS). Unlike tDCS, tACS can lead to physiological entrainment at frequency of stimulation which can provide physiological insights based on grey-box modeling.

In summary, our study presented a preliminary investigation of linear systems analysis using a physiologically-constrained grey-box model that was found useful to explore various pathways in a lumped NVU model related to CVR to HD-tDCS. Such grey-box linear systems analysis using fNIRS-tHb data from individuals with pathological conditions⁶¹ can elucidate dysfunction in various NVU pathways, e.g., due to the pathological infestation. Here, our proposed linear systems analysis using the grey-box model is amenable to pole-zeros analysis of the transfer function for various pathways of the neurovascular system in health, aging, and disease that can also be used to classify the dysfunction²⁶. This is crucial since neurovascular coupling dynamics are complicated phenomena in humans, and it can be hard to uncouple neuronal and vascular effects without mechanistic model-based hypothesis testing. The association between neuronal activity and hemodynamic responses can also be indirectly examined through other functional neuroimaging techniques such as fMRI and PET. Here, the integration of tDCS with functional neuroimaging modalities holds immense promise for throwing light on the underlying neuromodulation processes of current density effects. Experimental studies have indicated that long-term tDCS tends to transform neuronal activity through an induced electric field modulation of the cortical neurotransmitters (like gamma-aminobutyric acid and glutamate) during tDCS^{24,64}. Besides, there is evidence of studies on CBF modulation through tDCS^{5,6,8}. Of the available functional neuroimaging technologies, fNIRS, a portable, noninvasive clinically available tool, allows monitoring the local cortical hemodynamic response with reasonable spatial resolution and better temporal resolution than the gold standard of fMRI. fNIRS provides a measurement of changes in the cerebral oxygenation (oxy-Hb and deoxy-Hb) and blood volume (sum of oxy-Hb and deoxy-Hb)^{65,66} that is a promising tool to evaluate CVR to tDCS as evident from several studies^{67,68}. The modality has been extensively used in various brain diseases like epilepsy, stroke, Parkinson's disease, and mild cognitive impairment over the last few decades⁶⁹. It can provide an indirect measure of CBF during tDCS where the advantage over other neuroimaging modalities like fMRI and PET are: portability, better safety, higher temporal resolution, and cost effectiveness⁷⁰. Also, fNIRS can be combined with tDCS with no electro-optic interference to measure hemodynamic response during electrical stimulation. Moreover, dosing of the tDCS-induced current density can be monitored for safety in a diseased state since the blood-brain barrier (BBB) dysfunction in severe cases⁷¹ can be worsened by an increased BBB permeability⁵³. Therefore, our study provided fNIRS based rational approach to investigate the underlying mechanism of the hemodynamic response to tDCS that is crucial for the clinical translation of transcranial electrical stimulation approaches in cerebrovascular diseases due to its ease of use and low cost^{72,73}. Also, fNIRS measurement of Cytochrome-C-Oxidase⁷⁴ has been shown feasible that is important due to the relation of vascular density and the cytochrome oxidase activity¹³.

Indeed, various studies have evaluated the hemodynamic effects of tDCS using fNIRS in humans in published literature. Merzagora et al.⁷⁵ assessed the changes in prefrontal cortical oxygenation related to tDCS using fNIRS in healthy participants at rest. A large increase in oxy-Hb was observed in the 10min period following anodal tDCS compared to baseline levels before tDCS. Muthalib et al.⁴⁴ showed that anodal HD-tDCS induced more significant increases in oxy-Hb significantly during 10min of stimulation (at 2mA) in the sensorimotor cortex region within the vicinity of the 4 x 1 HD-tDCS montage compared to the region outside this boundary. At the same time, there were minimal oxy-Hb changes in the contralateral non-stimulated sensorimotor cortex region. Yaqub et al.⁷⁶ evaluated the prefrontal cortex resting-state intra-hemispheric and inter-hemispheric connectivity changes induced by 10min (1mA) anodal 4x1 HD-tDCS in healthy participants. Also, network connectivity changes were observed by analyzing filtered oxy-Hb time-series signals using standard graph theory metrics. Compared to the pre-stimulation phase, Yaqub et al.⁷⁶ observed that the oxy-Hb levels and the resting-state connectivity of the prefrontal cortex increased during and after the stimulation, and the connectivity changes were more significant in the vicinity of the 4x1 HD-tDCS electrodes. Sood et al.⁴² extended Dutta et al.⁶¹ study and presented an autoregressive model parameter estimator method using Kalman filter to evaluate the relationship between changes in the fNIRS oxy-Hb signal and the EEG bandpower signal during anodal HD-tDCS. The time-varying poles of the autoregressive model were found to be comparable in all the healthy participants. In contrast, the zeros of the model exhibited variations across the participants during HD-tDCS.

Limitations of this study included the methodical limitations of the fNIRS technique⁷⁷. The fNIRS signal acquired with optodes placed on the scalp can represent different hemodynamic signal sources (cerebral versus extra-cerebral) and other physiological causes (neuronal versus systemic) that can be evoked by tDCS. Due to the lack of short-separation channels to perform short source-detector regression to remove extra-cerebral hemodynamics, we performed a data-driven principal component analysis to identify the extra-cerebral signal components that explained the most significant amount of covariance across all the 16 spatially symmetrically distributed fNIRS channels. We found that Pathway 3 presented the least MSE, as shown in Fig. 4, so the fNIRS-tHb signal is postulated to have a significant representation from the superficial pial vessels. Differential activation of the oxy-Hb and deoxy-Hb (see section D: Oxy and Deoxy-Hemoglobin Changes at the Stimulated Region of the supplementary materials) also indicated neuronal activation and “metabolic hypothesis” for the cerebral capillaries in the vicinity of the HD-tDCS electrodes, which was used as a marker of neuronal cause. During grey-box modeling, the physiologically detailed model was substantially simplified by model linearization that lost nonlinear system dynamics, where calcium dynamics may be necessary for understanding the effects of tDCS on the rhythmic oscillations in the frequency range of 0.05–0.2 Hz⁶³. Such rhythmic nonlinear calcium dynamics are postulated to be affected by tDCS current density, which will be investigated in our future study by adding the nonlinear calcium dynamics to our linear model. In this study, the parameterized grey-box linear model was fitted to slow transients in 0.01 and 0.05 Hz of fNIRS tHb, since we performed downsampling to 0.1 Hz that removed oscillations in the frequency range of 0.05–0.2 Hz. So, our investigation considered the acute

effects of anodal tDCS by considering potassium ions as the main vasoactive agent with lumped multi-compartmental model of NVU.

Methods

(A) Participants and the Experimental Protocol

Eleven healthy participants (1 female, 19–45 years old) voluntarily participated after informed consent in this study, which received ethics approval by the Institutional Review Board of Euromov (University of Montpellier, France), and in accordance with the Declaration of Helsinki. The participants had no known neurological or psychiatric history, nor any contraindications to tDCS. In this study, the pilot data from our prior work on online parameter estimation with an autoregressive model⁴² was analyzed with a grey-box model for a mechanistic understanding of the tDCS action on total hemoglobin.

During the experiment, the participants were comfortably seated with eyes-open in an armchair with adjustable height. The set-up of the high-definition (HD) tDCS electrodes and fNIRS optodes were mounted on the surface of the scalp according to the 10/10 system (see Fig. 6). The anodal HD-tDCS (StarStim, Neuroelectronics NE, Barcelona, Spain) was configured in a 4×1 ring montage with the anode placed in the center (C3) in a region overlying the left primary sensorimotor cortex. The return electrodes were placed approximately 4 cm away at FC1, FC5, CP5, and CP1 in the 10/10 system (see Fig. 6). In the rest of the document, 'HD-tDCS' means 'anodal HD-tDCS' since we only performed anodal tDCS for this human pilot study. Measurements of changes in eyes-open resting-state oxy-hemoglobin (oxy-Hb) and deoxy-hemoglobin (deoxy-Hb) concentrations from the bilateral primary sensorimotor cortex were made from a 16-channel continuous-wave NIRS system (OxyMonMkIII, Artinis Medical Systems, Zetten, The Netherlands) at a sampling frequency of 10 Hz. The receiver-transmitter distance of 3 cm was based on our prior work⁴². The receivers (Rx) were placed on the FC3 and CP3 for the left hemisphere and FC4 and CP4 for the right hemisphere. Transmitters (Tx) were placed diagonally, i.e., at P1, P5, C1, C5, F5, and F1 for the left hemisphere, and P6, P2, C6, C2, F2, and F6 for the right hemisphere, as shown in Fig. 6. The HD-tDCS was conducted using Pistim (Neuroelectronics NE, Barcelona, Spain) electrodes (contact area 3.14cm^2) over the left primary motor cortex region to deliver 2mA current for 10 minutes, with a ramp up and ramp down of 30 seconds. Eyes-open resting-state data for changes in oxy-Hb and deoxy-Hb was recorded. The effect of HD-tDCS on blood volume was considered for the grey-box linear modeling, so the average values of tHb concentration change ($= \text{oxy-Hb} + \text{deoxy-Hb}$) were obtained from the optodes in the vicinity of 4×1 HD-tDCS electrodes: C5-CP3, C1-CP3, C5-FC3, and C1-FC3, as well as from contralateral non-stimulated hemisphere (C2-FC4, C2-CP4, C6-FC4, and C6-CP4). The first criterion to confirm the signal quality was a visual inspection for the presence of cardiac pulsation, in either the time or the frequency domain (peak around 1Hz cardiac frequency).

Due to the lack of short-separation channels to perform short source-detector regression to remove extra-cerebral hemodynamics, we performed data-driven principal component analysis (PCA) to identify the signal components that explained the greatest amount of covariance across all the spatially

symmetrically distributed 16 channels. This pre-processing of the fNIRS data was performed with HOMER2 (v2.2) routines (hmrIntensity2OD and hmrOD2Conc, respectively) using the modified Beer-Lambert law and their standard pipeline. Specifically, motion correction (hmrMotionCorrectWavelet) and zero-phase bandpass filtering ("hmrBandpassFilt") was performed to extract the frequencies between 0.01 Hz and 0.1 Hz across all the 16 channels. Here, the PCA approach was applied to improve the signal to noise ratio towards neurovascular and neurometabolic coupling than systemic physiology⁷⁸. The neurovascular and neurometabolic coupling-related hemodynamic response should lead to an initial increase in deoxy-Hb and an equal decrease in oxy-Hb, as shown by Devor et al.¹⁰. Then, the blood volume should start to increase about 600ms following the neural stimulus¹⁰. Such differential activation of oxy-Hb and deoxy-Hb was found in the vicinity of 4x1 HD-tDCS electrodes: C5-CP3, C1-CP3, C5-FC3, and C1-FC3, that indicated neurovascular coupling related hemodynamic response by HD-tDCS current density at the ipsilateral primary motor cortex. Therefore, the fNIRS channels were analyzed for the negative correlation between oxy-Hb and deoxy-Hb dynamics for each participant that is based on the rationale for correlation-based signal improvement⁵⁰ for the contrast to noise ratio (see Supplementary Table S2 in the supplementary materials). We also investigated the fNIRS time series data at the contralateral sensorimotor area that was not directly affected by the HD-tDCS current density confirmed using finite element modeling (see Fig. 7(A)). Here, current spread (section H: Electric Field in brain tissues in the supplementary materials) in the highly conductive (mean 1.69 S/m²⁹) CSF to tissue boundary compared to grey matter (mean 0.60 S/m²⁹), blood (mean 0.58 S/m²⁹), and vessel wall (0.46 S/m²⁹) can lead to a spatial change in the tangential surface current (J_{Tin}), e.g., along the pial surface (see Fig. 7(C)), resulting in the activating function for perivascular nerves. We have postulated⁴² the HD-tDCS current density's propensity to affect the autonomic nerves in the adventitial layer – see Fig. 7(B). Here, low-frequency vessel oscillations were considered related to the interplay between neurovascular coupling and vasomotor control based on prior works^{55,79,80}. In this study, the grey-box linear model did not capture nonlinear calcium dynamics in the low-frequency (0.05–0.2 Hz), so we investigated the lower frequency (0.01–0.05Hz) slower transient for fitting fNIRS data within the first 150 sec of the HD-tDCS (30sec ramp-up and 2 min steady-state).

(B) Detailed physiological model selection

Various mathematical models representing the NVU mechanisms with major compartments – neuron, astrocyte, and vascular cells – have been published. A description of these published mathematical models is given in Table 3. These models are constructed using physical, electrical, and hemodynamics laws tied with experimental analysis to demonstrate the signaling in different NVU cell constituents. The inter-compartmental dynamics are represented by a set of differential equations having compartment-specific variables. The initial models were presented by Bennett et al.⁴⁸ and Farr and David⁴⁷ that used synaptic space, astrocyte, smooth muscle cell, perivascular space and endothelial cells as components of a neurovascular system. The study presented the coupling between neuronal activation (through K⁺ and glutamate) and arteriolar dilation via astrocytic potassium ions (K⁺), epoxyeicosatrienoic acids (EETs),

and calcium ion (Ca^{2+}) channels. Afterward, studies by different researchers^{38,81-83} broadened the basic models by augmenting various physiological segments and detailing the NVU mechanisms.

Table 3. Summary of studies detailing mathematical models of the neurovascular unit (NVU) components and their input (I) and output (O)

S. No.	Study	NVU system	Description
1	Bennett et al., 2008 ⁴⁸	Synaptic space, astrocyte, SMC; I: Glutamate released from glutamatergic synapse; O: Cerebral blood volume	The study showed that the coupling between glutamatergic synapses to arteriolar SMC is mediated by astrocytic epoxyeicosatrienoic acids (EETs). Results depicted a linear rise in blood flow with an increase in numbers of activated astrocytes; however, the response was non-linear with respect to the release of glutamate.
2	Farr and David, 2011 ⁴⁷	Synaptic space, astrocyte, perivascular space, SMC, and endothelial cells; I: Glutamate and potassium in synaptic space; O: arteriolar diameter	The study showed that the coupling between neuronal activation (due to K ⁺ and glutamate) to arteriolar dilation was mediated by astrocytic K ⁺ , EET, and Ca ²⁺ .
3	Witthoft and Karniadakis, 2012 ³⁸	Synaptic space, astrocyte, perivascular space, SMC; I: Glutamate and potassium in synaptic space; O: vessel circumference	The study showed the bidirectional communication between cerebral astrocytes and the microvessels. Major signaling pathways considered were: neural synaptic K ⁺ and glutamate to astrocytes, K ⁺ signaling between astrocytes and microvasculature, and microvasculature to astrocytes via astrocyte perivascular endfoot.
4	Chander and Chakravarthy, 2012 ⁸⁴	Neuron, astrocyte, vessel, and interstitium; I: Synaptic current and Adenosine Triphosphate (ATP); O: vessel radius	The study presented a model for the neuron-astrocyte-vessel loop based on neuronal and metabolic activity.
5	Witthoft et al., 2013 ⁸⁵	Synaptic space, astrocyte, perivascular space, SMC; I: Glutamate and potassium in synaptic space; O: arteriole radius	Extended version of the model from Witthoft and Karniadakis, 2012 ³⁸ with potassium buffering across all components of NVU.
6	Chang et al., 2013 ⁸⁶	Soma, dendrite, extracellular space, vascular tree compartment, glial compartment; I: extracellular potassium; O: vessel radius	The study demonstrated the coupling between the vascular diameters and neuronal activity mediated by potassium concentrations in extracellular space in the vicinity to dendritic processes that were assumed to be buffered through astrocytes.
7	Dormanns et al., 2015 ⁸⁷	Neuron, synaptic cleft, astrocyte, perivascular space, SMC, endothelial cell, and arteriolar lumen; I: synaptic potassium; O: arteriole radius	The study used lumped model of the NVU for depicting the connection between a neuron and the perfusing arteriole through the astrocytic perivascular K ⁺ signaling and the SMC's Ca ²⁺ dynamics. The study showed the significance of luminal agonists in flowing blood influencing the endothelial and SMC dynamics.
8	Dormanns et al., 2016 ⁸¹	Neuron, synaptic cleft, astrocyte, perivascular space, SMC, endothelial cell, and arteriolar lumen; I: synaptic potassium; O: arteriole radius	An extended version of Dormanns et al., 2015 model ⁸⁷ with NO signaling pathway. The model considered the production of NO in the neuron and the endothelial cell compartments and its diffusion in the other compartments.
9	Chhabria and Chakravarthy, 2016 ⁸⁸	Neuron lumped gliovascular subsystem; I: neural firing rate; O: energy variable (ATP)	The study presented a low dimensional model of the previous model (Chander and Chakravarthy, 2012 ⁸⁴) in which the gliovascular system was merged into a single subsystem.
10	Blanchard et al., 2016 ⁸⁹	Pyramidal cells, interneurons, extracellular space, astrocytes, vessels; I: Firing rates from pyramidal cells and interneurons; O: local field potential and regional cerebral blood flow	The study demonstrated the connection between the neuronal activity and regional CBF via neuro-glio-vascular link at the population scale (voxel). The model evaluated the role of astrocytes in glutamate and GABA recycling, which then influences adjoining vessels
11	Mathias et al., 2017 ⁹⁰	Soma, dendrite, extracellular space, synaptic space, astrocyte, perivascular space, SMC,	The study demonstrated the signaling method of neurovascular coupling through a model of pyramidal neurons and its analogous fMRI BOLD response. The study extended the NVU to include a

		endothelial cell and lumen; I:neural activation through ion channels; O: fMRI BOLD signal	complex neuron system with Na/K ATPase pump mechanism, which provides CBF and cerebral metabolic rate of oxygen (CMRO ₂).
12	Kenny et al., 2018 ⁸²	Neuron, synaptic cleft, astrocyte, perivascular space, endothelial cell, SMC, and lumen; I: Glutamate and potassium in synaptic space; O: arteriolar radius	The model used lumped parameter systems to depict the connection between a neuron and perfusing arteriole through the astrocytic perivascular K ⁺ and the SMC's Ca ²⁺ dynamics mediated by astrocytic EETs and TRPV4. Results indicated that K ⁺ mediated pathway drives the quick start of vaso-dilation compared to the NO-mediated pathway.
13	Mathias et al., 2018 ⁸³	Neuron (soma, dendrite), extracellular space, synaptic space, astrocyte, perivascular space, SMC, endothelial cell and lumen; I:neuronal current; O: fMRI BOLD signal	The model simulated NVU mechanisms and BOLD signal by extending the previous models by Mathias et al., 2017 ⁹⁰ and Kenny et al., 2018 ⁸² . The study included a transient sodium ion channel in the neuron compartment.
14	Sten et al., 2020 ⁹¹ .	Pyramidal neuron, GABAergic interneuron, SMC, arteriole; I:neuronal pulse mediating vaso-agents; O: arteriolar diameter	The study modeled the interplay between pyramidal neurons and GABAergic interneurons in the NVU. The study evaluated the role of cell-specific contributions in NVU due to the effect of an anesthetic agent.

We selected the physiologically detailed model by Witthoft and Karniadakis³⁸ since their study showed the bidirectional communication between cerebral astrocytes and microvessels, which was relevant due to experimental results that astrocytes are susceptible to small variations in their membrane potential⁹², and their long processes are sensitive to polarization by tDCS⁹³⁻⁹⁵. In Fig. 8, we compared the Witthoft and Karniadakis³⁸ model with two recent models, Kenny et al.⁸², which depicted the connection between neurons and perfusing arteriole through the astrocytic perivascular K⁺ and the SMC's Ca²⁺ dynamics, and Mathias et al.⁸³ model that extended Kenny et al., 2018⁸² model as explained in Table 3. For comparison of the model responses, the models were simulated using the 'ode23tb' solver in Simulink (MathWorks, Inc., USA), and the normalized vessel radius change was considered during a neuronal stimulus between 30 to 70 sec as shown in Fig. 8. We found that the physiologically detailed model by Witthoft and Karniadakis³⁸ generated vessel oscillations driven by non-linear calcium dynamics and bidirectional communication between cerebral astrocytes and microvessels. Also, Witthoft and Karniadakis³⁸ model had a quick start of the vasodilation comparable to Mathias et al.⁸³ model that extended Kenny et al., 2018⁸² model. Witthoft and Karniadakis³⁸ model also captured the after-effect of the neuronal stimulation on the normalized vessel radius. However, such detailed physiological model (section A: Model Equations for Neurovascular Compartmental Dynamics in the supplementary material) may be unidentifiable, i.e., characterized by many parameters that are poorly constrained by limited experimental data from low-density fNIRS studies in human.

(C) Physiologically detailed Neurovascular Compartmental Dynamics

Table 4. State variables of the pathways for tDCS effects in the lumped model of the neurovascular unit for physiologically detailed modeling from published literature^{38,47-49}

Compartments of the lumped model of the neurovascular unit			
Synaptic Space	Intracellular Astrocyte Space	Perivascular Space	Arteriole smooth muscle cell (SMC) Intracellular Space
Potassium concentration in the synaptic space (<i>potassium_s</i>)	Astrocytic Inositol trisphosphate (<i>ip3</i>)	Perivascular potassium concentration, (<i>potassium_p</i>)	Open KIR (Inward Rectifying Potassium) channel probability (<i>k</i>)
	Astrocytic intracellular calcium concentration, (<i>calcium_a</i>)		SMC Membrane Potential (<i>V_m</i>)
	Gating variable (<i>h</i>)	Perivascular calcium concentration (<i>calcium_p</i>)	Open potassium channel probability (<i>n</i>)
	TRPV4 (Transient Receptor Potential Vanniloid Related 4) channel open probability (<i>ss</i>)		Calcium concentration in the SMC (<i>calcium_smc</i>)
	Calcium-dependent EET (Epoxyeicosatrienoic Acid) production in the cell (<i>eet</i>)		The fraction of attached cross-bridges (<i>omega</i>)
	Open BK(Big Potassium) channel probability (<i>nbk</i>)		Normalized contractile component of length (<i>yy</i>)
	Astrocyte Membrane Potential (<i>V_k</i>)		Mean circumference of the vessel (<i>x</i>)

A detailed mathematical model of tDCS effects on the NVU was simulated based on published literature^{38,47-49} (see Table 3), as shown by the anatomical representation in Fig. 9(A) and block diagram in Fig. 9(B). The state variables in the compartments of the lumped model of the NVU are tabulated in Table 4. Besides neurons, the major non-neuronal glial cells in the brain, astrocytes, are also susceptible to small variations in their membrane potential⁹², and their long processes are sensitive to polarization by tDCS⁹³⁻⁹⁵. In animal studies, tDCS has been found to induce astrocytic calcium waves in the visual cortex to steer plasticity of the visually evoked potentials⁹⁶. Further, electrically coupled populations of glial cells, known as a glial syncytium, can intensify field polarization in response to tDCS. Glial cells maintain extracellular potassium concentration by the imbalance in their membrane polarity and can affect potassium spatial buffering through tDCS modulation^{32,97}. Likewise, vascular cells such as endothelial cells and arteriolar SMC can be affected by tDCS through the modulation of nitric oxide (NO) mediates, alignment and angiogenesis in endothelial cells, and polarization of SMC causing vasomotion via metabolites such as potassium ions (K⁺), adenosine, NO and calcium ions (Ca²⁺)^{98,99}. Our model developed from the physiologically detailed models by Witthoft and Karniadakis³⁸ and Kenny et al., 2018⁸² models, thereby presented Witthoft and Karniadakis³⁸ generated vessel oscillations with the Kenny et al., 2018⁸² models' K⁺ mediated pathway to drive rapid vasodilation at tDCS onset – see Fig. 8 for the model simulations. Neuronal effects due to tDCS current density will take an intricate path to the synaptic transmembrane current, considering only excitatory effects that can be mapped through a sigmoid function as presented by Molae-Ardekani et al.¹⁰⁰. In this current study, we did not explicitly

model neuronal dynamics, so we did not capture neuroplastic changes²⁴ and excitability after-effects induced by longer duration (> 3 min) tDCS. To capture the immediate effects of tDCS, the major vasoactive signaling pathways were solely considered in our model, viz., neural synaptic potassium (K+) and glutamate to astrocytes, K+ signaling between astrocytes and microvasculature, and microvasculature to astrocytes interactions via astrocyte perivascular endfoot³⁸. The detailed differential equations and model parameters are provided in the supplementary materials (see section A: Model Equations for Neurovascular Compartmental Dynamics). Our goal was mechanistic modeling for hypothesis testing, where the hypotheses are formulated as a set of mathematical equations for data fitting to identify core predictions from our biological criteria¹⁰¹. We identified four nested pathways (see Fig. 10) starting from a state variable at one of the four NVU compartments (see Table 4) based on our biological criteria¹⁰¹ to capture tDCS effects on the blood vessel (circumference). Figure 10 shows the nested model for each of the four pathways starting from tDCS current where one of the models could be obtained by fixing or eliminating parameters in another model. The tDCS current density in the brain's neurovascular tissue was assumed to be proportional to the tDCS current applied at the scalp due to the Ohmic volume conductor head model (see section A, Transcranial electrical stimulation-induced current density in the neurovascular cortical tissue in the supplementary materials). Pathway 4 model from the arteriole SMC intracellular space postulated tDCS current density effects on the SMC's voltage-gated current channel via a first-order transfer function cascaded with the NVU model. Pathway 3 model adds a path to the Perivascular Space where tDCS current density was postulated to affect the perivascular potassium concentration via a first-order transfer function. Pathway 2 model adds a path to the Astrocytic Intracellular Space where tDCS current density was postulated to affect the astrocytic transmembrane current via a first-order transfer function. Then, Pathway 1 model adds a path to the Synaptic Space where the potassium release from active neurons was modulated by tDCS current density via a first-order transfer function. Complete Pathway, 1 model dynamics, were represented by seventeen ordinary differential equations that nested Pathways 2–4 – see Fig. 10. The synaptic activity was assumed to be modulated by tDCS current density¹⁰² that affected potassium release from active neurons into the synaptic space. In Pathway 1, the vasoactive signal-induced activation of downstream neurovascular coupling pathways leading to the acute hemodynamic (tHb) effects of tDCS. Studies have shown that potassium ions can act as a potent vasodilator signal that couples local neuronal activity to vasodilation in the brain, and have a major role in cerebrovascular mechanisms^{56,103–105}. Studies have shown that the potassium pathway is responsible for the fast onset of vasodilation compared to the other mediators^{82,83,106}. In our model, the induced current density in the Ohmic volume conductor head model was assumed to have a vasoactive influence not only on potassium release into the synaptic space but also at different downstream compartments, as listed in Table 4. Indeed, prior works have shown the change in the concentration of various vasoactive agents like adenosine, nitric oxide (NO), potassium (K+) can be represented as a vasoactive signal with first-order Friston's model¹⁰⁷. In this study, tDCS current density in the neurovascular brain tissue induced vasoactive signal starting at one of the four compartments via a first-order linear filter cascaded with the NVU model hypothesis testing as shown in Fig. 10. The tDCS current at the scalp (I_{tdcs}) was proportional (leadfield – see the section A in

the supplementary materials on Transcranial electrical stimulation induced current density in the neurovascular cortical tissue) to current density (J_{tDCS}) in the neurovascular brain tissue leading to the vasoactive signal via first order transfer function,

$$v = \frac{K}{s/\tau+1} I_{tdcs} \quad (1)$$

where K is arbitrary gain from leadfield ($J_{tDCS} = K \cdot I_{tdcs}$), and τ is the time constant fitted to fNIRS data.

The state variables for various compartments of the neurovascular unit used in the present study are listed in Table 4, while the detailed equations are provided in the supplementary materials (see section A: Model Equations for Neurovascular Compartmental Dynamics).

(D) Participant-specific Grey-box Linear Model Dynamics

In our current study, a grey-box linear model was developed from a detailed physiological model to analyze tDCS-evoked tHb changes for hypothesis testing. Although the detailed non-linear model can be fitted using advanced methods, e.g., simulated annealing (Optimization Toolbox - MATLAB – MathWorks, USA); however, simplifying the model is necessary to identify key mechanisms of the system and to understand relevant aspects as shown as pathways in Fig. 10. Therefore, we applied grey-box linear modeling where many states and parameters were removed for the identification of the core predictions based on our biological criteria¹⁰¹. Grey-box models can be evaluated using experimental data fitting based on the cost function that sums the squared and normalized residuals. In this current study, the lumped model of the NVU assumed a system of input (vasoactive signal from tDCS - "equation (1)") and outputs (change in terms of vessel circumference). The dynamics of NVU were considered through chemical signaling mechanisms across four compartments, as shown in Fig. 10. For modeling the vessel function and hemodynamics, a cylindrical vessel component having a unit length was considered as a lumped model of the blood vessel^{38,49}. The vessel circumference changes as the NVU model's output was mapped to the tHb (or blood volume) time series by the vessel volume function block in Fig. 10. Under the assumption of small circumference changes due to tDCS vasoactive action, the blood volume changes were assumed to be proportional to the vessel circumference. Here, changes in tHb were considered proportional to the blood volume¹⁰⁸, so lumped volume response using vessel circumference was mapped to the tHb changes under small change approximations.

Figure 11 shows our grey-box model estimation flow diagram using System Identification Toolbox (MathWorks, Inc., USA). The grey-box linear modeling of the four pathways from the physiologically detailed neurovascular coupling model was performed using the Simulink (MathWorks, Inc., USA) linear analysis tool. This tool allowed the linearization of complex nonlinear models at the baseline operating point of the physiologically detailed NVU model^{38,47-49}. Therefore, the linearized grey-box model was constrained by the physiology of the respective four pathways (see Fig. 10) and compartments in the physiologically detailed NVU model (see Table 4). The grey-box linear model with identifiable free parameters ('idgrey' in MATLAB) was updated using the "Refine Existing Model" approach ('greyest' for

'idgrey' model) in the System Identification Toolbox (MathWorks, Inc., USA) that uses prediction-error minimization algorithm ('pem' in MATLAB) to update the parameters of the initial model to improve the fit to the estimation data, as shown in Fig. 11. The model evaluation was based on the properties of the prediction-error cost function for each pathway (i.e., our hypothesis) and the residuals for each participant, i.e., pathway-specific and participant-specific mean squared error (MSE).

(E) Investigation of the Four Pathways/Hypotheses using a Reduced Dimension Grey-box Linear Model

The linearized grey-box model's complexity from the physiologically detailed neurovascular coupling model states (see Table 4) was simplified with reduced-order approximations using the Model Reducer app in the Control System Toolbox (MathWorks, Inc., USA). Simpler models can preserve model characteristics while discarding states that contribute relatively little to system dynamics (Balanced Truncation Model Reduction, 'balred' in MATLAB). Simpler transfer function models can provide insights into the linear time-invariant model dynamics that were derived from the minimal realization transfer function for the four pathways. A generic reduced dimension grey-box linear model was derived ('tfest' in MATLAB) using the nested linearized grey-box models for the initial parameterization – see Fig. 11. Average tHb time series during initial 150 sec of HD-tDCS from eight good participants (participants 3, 4, 10 were rejected due to > -0.5 correlation coefficient between oxy-Hb & deoxy-Hb at the stimulated sensorimotor cortex – see Supplementary Table S2) was used for model fitting. We used Chi-Square Goodness-of-Fit for comparing the four hypotheses (as minimal realization transfer function) for the nested pathways (see Fig. 10), where Chi-Square difference test¹⁰⁹ determined the best pathway model of the least order.

Declarations

Author Contribution

Y.A. performed physiological modeling under the supervision of A.D. and S.R.C. that was motivated by original assessment (fNIRS-EEG) by A.D. of dysfunctional neurovascular coupling during tDCS in ischemic stroke. A.D. and M.H. conceived systems approach for the investigation of neurovascular coupling. P.W. performed electric field, and photon migration simulations under the supervision of A.D. A.D., M.H., M.M., and S.P. supervised design and implementation of healthy human studies. Y.A. took the lead in writing the manuscript under the supervision of A.D. All authors provided critical feedback and helped shape the research, analysis, and manuscript.

Competing Interests Statement

Dr. Muthalib reports personal fees from Silverline Research, outside the submitted work; Dr. Muthalib did not at any time receive payment or services from Silverline Research for any aspect of the submitted work (including but not limited to grants, data monitoring board, study design, manuscript preparation, statistical analysis, etc.). Other author declare no competing interests.

Acknowledgments

The authors would also like to acknowledge the help of Ms. Mehak Sood, Mr. Utkarsh Jindal, and Dr. Pierre Besson for the human study.

Compliance with ethical standards

Funding: The computational work is funded by the Indian Institute of Technology Mandi, Science and Engineering Research Board (SERB), a statutory body of the Department of Science and Technology, Government of India and, Ministry of Electronics and Information Technology (MeitY), Government of India. Community for Global Health Equity (CGHE) at the University at Buffalo also partly supported this study.

Ethical approval: This study received Ethics approval by IRB of Euromov (University of Montpellier, France) and in accordance with the Declaration of Helsinki.

References

1. Kisler, K., Nelson, A. R., Montagne, A. & Zlokovic, B. V. Cerebral blood flow regulation and neurovascular dysfunction in Alzheimer disease. *Nature Reviews Neuroscience*.**18**, 419 (2017).
2. Millikan, C., CH, M. & RB B. A classification and outline of cerebrovascular diseases II. (1975).
3. Pan, Y., Li, H., Wardlaw, J. M. & Wang, Y. A new dawn of preventing dementia by preventing cerebrovascular diseases. *bmj***371** (2020).
4. International, A. s. D. (Alzheimer's Disease International London, UK 2019).
5. Zheng, X., Alsop, D. C. & Schlaug, G. Effects of transcranial direct current stimulation (tDCS) on human regional cerebral blood flow. *Neuroimage*.**58**, 26–33 (2011).
6. Pulgar, V. M. Direct electric stimulation to increase cerebrovascular function. *Frontiers in systems neuroscience*.**9**, 54 (2015).
7. Dutta, A. Bidirectional interactions between neuronal and hemodynamic responses to transcranial direct current stimulation (tDCS): challenges for brain-state dependent tDCS. *Frontiers in systems neuroscience*.**9**, 107 (2015).
8. Jamil, A. *et al.* Current intensity-and polarity-specific online and aftereffects of transcranial direct current stimulation: An fMRI study. *Hum. Brain. Mapp*.**41**, 1644–1666 (2020).
9. Turner, D. A. *et al.* Dose-Dependent Enhancement of Cerebral Blood Flow by transcranial AC Stimulation in Mouse. *Brain Stimul*.**14**, 80–87 (2020).
10. Devor, A. *et al.* Coupling of total hemoglobin concentration, oxygenation, and neural activity in rat somatosensory cortex. *Neuron*.**39**, 353–359 (2003).
11. Zhang, J. H. *et al.* The vascular neural network—a new paradigm in stroke pathophysiology. *Nature Reviews Neurology*.**8**, 711–716 (2012).

12. Echagarruga, C. T., Gheres, K. W., Norwood, J. N. & Drew, P. J. nNOS-expressing interneurons control basal and behaviorally evoked arterial dilation in somatosensory cortex of mice. *Elife*.**9**, e60533 (2020).
13. Schmid, F., Barrett, M. J., Jenny, P. & Weber, B. Vascular density and distribution in neocortex. *Neuroimage*.**197**, 792–805 (2019).
14. Khadka, N., Bikson, M. & Neurocapillary-Modulation *Neuromodulation: Technology at the Neural Interface* (2020).
15. Workman, C. D., Fietsam, A. C., Ponto, L. L. B., Kamholz, J. & Rudroff, T. Individual Cerebral Blood Flow Responses to Transcranial Direct Current Stimulation at Various Intensities. *Brain sciences*.**10**, 855 (2020).
16. Nitsche, M. A. & Paulus, W. Excitability changes induced in the human motor cortex by weak transcranial direct current stimulation. *The Journal of physiology*.**527**, 633–639 (2000).
17. Bikson, M. *et al.* Safety of transcranial direct current stimulation: evidence based update 2016. *Brain stimulation*.**9**, 641–661 (2016).
18. Huang, Y. *et al.* Measurements and models of electric fields in the in vivo human brain during transcranial electric stimulation. *Elife*.**6**, e18834 (2017).
19. Datta, A. *et al.* Gyri-precise head model of transcranial direct current stimulation: improved spatial focality using a ring electrode versus conventional rectangular pad. *Brain stimulation* **2**, 201–207. e201(2009).
20. Rahman, A. *et al.* Cellular effects of acute direct current stimulation: somatic and synaptic terminal effects. *The Journal of physiology*.**591**, 2563–2578 (2013).
21. Wagner, T. *et al.* Transcranial direct current stimulation: a computer-based human model study. *Neuroimage*.**35**, 1113–1124 (2007).
22. Miranda, P. C., Lomarev, M. & Hallett, M. Modeling the current distribution during transcranial direct current stimulation. *Clinical neurophysiology*.**117**, 1623–1629 (2006).
23. Reato, D., Rahman, A., Bikson, M. & Parra, L. C. Effects of weak transcranial alternating current stimulation on brain activity—a review of known mechanisms from animal studies. *Frontiers in human neuroscience*.**7**, 687 (2013).
24. Stagg, C. J. & Nitsche, M. A. Physiological basis of transcranial direct current stimulation. *The Neuroscientist*.**17**, 37–53 (2011).
25. Guhathakurta, D. & Dutta, A. Computational pipeline for NIRS-EEG joint imaging of tDCS-evoked cerebral responses—an application in ischemic stroke. *Frontiers in neuroscience*.**10**, 261 (2016).
26. Westcott, E. B. & Segal, S. S. Perivascular innervation: a multiplicity of roles in vasomotor control and myoendothelial signaling. *Microcirculation*.**20**, 217–238 (2013).
27. Andersen, A. V., Simonsen, S. A., Schytz, H. W. & Iversen, H. K. Assessing low-frequency oscillations in cerebrovascular diseases and related conditions with near-infrared spectroscopy: a plausible method for evaluating cerebral autoregulation? *Neurophotonics* **5**, 030901(2018).

28. Blinder, P., Shih, A. Y., Rafie, C. & Kleinfeld, D. Topological basis for the robust distribution of blood to rodent neocortex. *Proceedings of the National Academy of Sciences* 107, 12670–12675(2010).
29. McCann, H., Pisano, G. & Beltrachini, L. Variation in reported human head tissue electrical conductivity values. *Brain topography*.**32**, 825–858 (2019).
30. Zlokovic, B. V. Neurodegeneration and the neurovascular unit. *Nature medicine*.**16**, 1370 (2010).
31. Huneau, C., Benali, H. & Chabriat, H. Investigating human neurovascular coupling using functional neuroimaging: a critical review of dynamic models. *Frontiers in neuroscience*.**9**, 467 (2015).
32. Bikson, M., Paulus, W., Esmaeilpour, Z., Kronberg, G. & Nitsche, M. A. in *Practical Guide to Transcranial Direct Current Stimulation* 81–113(Springer, 2019).
33. Pelletier, S. J. *et al.* The morphological and molecular changes of brain cells exposed to direct current electric field stimulation. *International Journal of Neuropsychopharmacology*.**18**, 090 (2015).
34. Dutta, A. *et al.* in *2013 6th International IEEE/EMBS Conference on Neural Engineering (NER)*. 827–830 (IEEE).
35. Duffin, J. *et al.* Cerebrovascular resistance: the basis of cerebrovascular reactivity. *Frontiers in neuroscience*.**12**, 409 (2018).
36. Markus, H. & Cullinane, M. Severely impaired cerebrovascular reactivity predicts stroke and TIA risk in patients with carotid artery stenosis and occlusion. *Brain*.**124**, 457–467 (2001).
37. Bouma, G. J. & Muizelaar, J. P. Cerebral blood flow, cerebral blood volume, and cerebrovascular reactivity after severe head injury. *J Neurotrauma*.**9**, S333–S348 (1992).
38. Witthoft, A. & Karniadakis, G. E. A bidirectional model for communication in the neurovascular unit. *Journal of Theoretical biology*.**311**, 80–93 (2012).
39. Chew, T., Ho, K. A. & Loo, C. K. Inter-and intra-individual variability in response to transcranial direct current stimulation (tDCS) at varying current intensities. *Brain Stimul*.**8**, 1130–1137 (2015).
40. López-Alonso, V., Cheeran, B. & Río-Rodríguez, D. & Fernández-del-Olmo, M. Inter-individual variability in response to non-invasive brain stimulation paradigms. *Brain stimulation*.**7**, 372–380 (2014).
41. Datta, A. Inter-individual variation during transcranial direct current stimulation and normalization of dose using MRI-derived computational models. *Frontiers in psychiatry*.**3**, 91 (2012).
42. Sood, M. *et al.* NIRS-EEG joint imaging during transcranial direct current stimulation: online parameter estimation with an autoregressive model. *Journal of neuroscience methods*.**274**, 71–80 (2016).
43. Scholkmann, F. *et al.* A review on continuous wave functional near-infrared spectroscopy and imaging instrumentation and methodology. *Neuroimage*.**85**, 6–27 (2014).
44. Muthalib, M., Besson, P., Rothwell, J. & Perrey, S. Focal hemodynamic responses in the stimulated hemisphere during high-definition transcranial direct current stimulation. *Neuromodulation: Technology at the Neural Interface*.**21**, 348–354 (2018).
45. Devor, A. *et al.* Frontiers in optical imaging of cerebral blood flow and metabolism. *Journal of Cerebral Blood Flow & Metabolism*.**32**, 1259–1276 (2012).

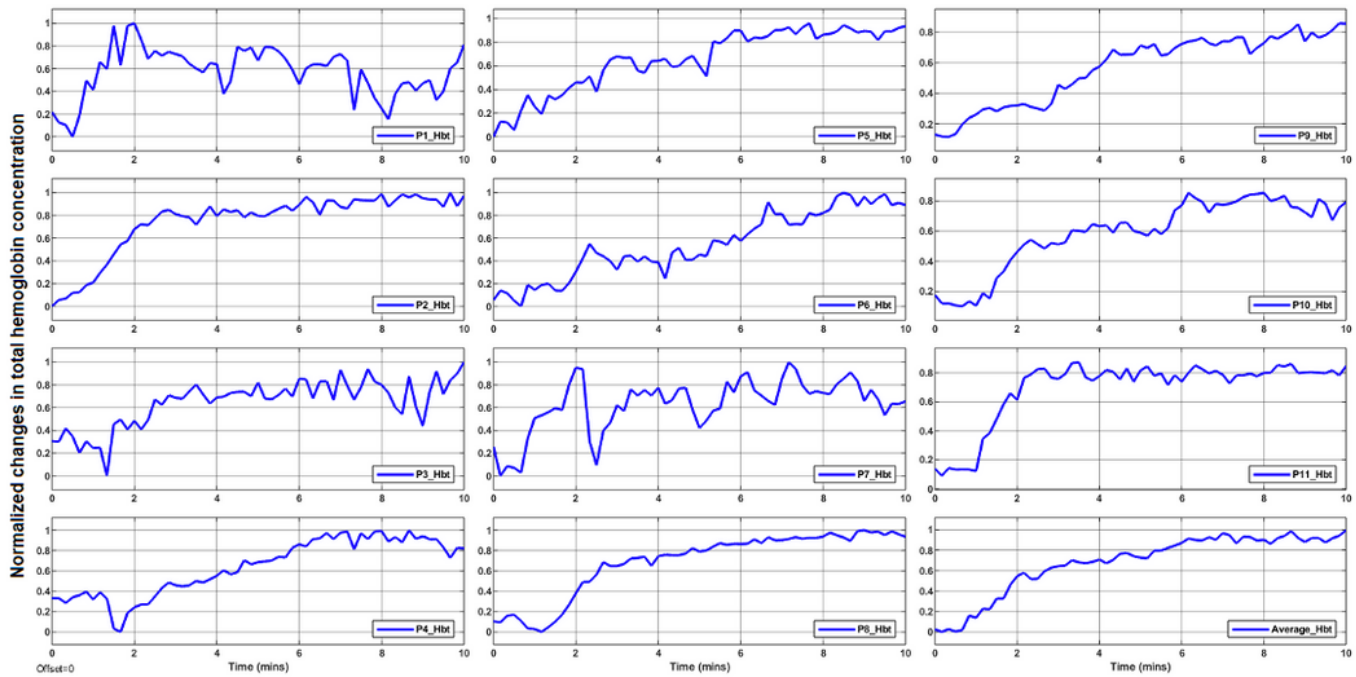
46. Villringer, A. & Chance, B. Non-invasive optical spectroscopy and imaging of human brain function. *Trends in neurosciences*.**20**, 435–442 (1997).
47. Farr, H. & David, T. Models of neurovascular coupling via potassium and EET signalling. *Journal of theoretical biology*.**286**, 13–23 (2011).
48. Bennett, M., Farnell, L. & Gibson, W. Origins of blood volume change due to glutamatergic synaptic activity at astrocytes abutting on arteriolar smooth muscle cells. *Journal of theoretical biology*.**250**, 172–185 (2008).
49. Gonzalez-Fernandez, J. M. & Ermentrout, B. On the origin and dynamics of the vasomotion of small arteries. *Mathematical biosciences*.**119**, 127–167 (1994).
50. Cui, X., Bray, S. & Reiss, A. L. Functional near infrared spectroscopy (NIRS) signal improvement based on negative correlation between oxygenated and deoxygenated hemoglobin dynamics. *Neuroimage*.**49**, 3039–3046 (2010).
51. Taylor, A. J., Kim, J. H. & Ress, D. Characterization of the hemodynamic response function across the majority of human cerebral cortex. *NeuroImage*.**173**, 322–331 (2018).
52. Buxton, R. B., Uludağ, K., Dubowitz, D. J. & Liu, T. T. Modeling the hemodynamic response to brain activation. *Neuroimage*.**23**, S220–S233 (2004).
53. Shin, D. W. *et al.* In Vivo Modulation of the Blood–Brain Barrier Permeability by Transcranial Direct Current Stimulation (tDCS). *Annals of Biomedical Engineering*,1–15(2020).
54. Laakso, I., Tanaka, S., Koyama, S., De Santis, V. & Hirata, A. Inter-subject variability in electric fields of motor cortical tDCS. *Brain stimulation*.**8**, 906–913 (2015).
55. Tan, Q. *et al.* Frequency-specific functional connectivity revealed by wavelet-based coherence analysis in elderly subjects with cerebral infarction using NIRS method. *Medical physics*.**42**, 5391–5403 (2015).
56. Kuschinsky, W., Wahl, M., Bosse, O. & Thurau, K. Perivascular potassium and pH as determinants of local pial arterial diameter in cats: a microapplication study. *Circul. Res*.**31**, 240–247 (1972).
57. Nieves-Cintrón, M., Syed, A. U., Nystoriak, M. A. & Navedo, M. F. Regulation of voltage-gated potassium channels in vascular smooth muscle during hypertension and metabolic disorders. *Microcirculation*.**25**, e12423 (2018).
58. Nelson, M. T. & Quayle, J. M. Physiological roles and properties of potassium channels in arterial smooth muscle. *American Journal of Physiology-Cell Physiology*.**268**, C799–C822 (1995).
59. Cedersund, G. & Roll, J. Systems biology: model based evaluation and comparison of potential explanations for given biological data. *The FEBS journal*.**276**, 903–922 (2009).
60. Jindal, U. *et al.* in 2015 37th Annual International Conference of the IEEE Engineering in Medicine and Biology Society (EMBC). 3399–3402 (IEEE).
61. Dutta, A., Jacob, A., Chowdhury, S. R., Das, A. & Nitsche, M. A. EEG-NIRS based assessment of neurovascular coupling during anodal transcranial direct current stimulation-a stroke case series. *Journal of medical systems*.**39**, 36 (2015).

62. Steffener, J., Tabert, M., Reuben, A. & Stern, Y. Investigating hemodynamic response variability at the group level using basis functions. *Neuroimage*.**49**, 2113–2122 (2010).
63. Rayshubskiy, A. *et al.* Direct, intraoperative observation of ~ 0.1 Hz hemodynamic oscillations in awake human cortex: implications for fMRI. *Neuroimage*.**87**, 323–331 (2014).
64. Stagg, C. J. *et al.* Polarity-sensitive modulation of cortical neurotransmitters by transcranial stimulation. *Journal of Neuroscience*.**29**, 5202–5206 (2009).
65. Owen-Reece, H., Smith, M., Elwell, C. & Goldstone, J. Near infrared spectroscopy. *British journal of anaesthesia*.**82**, 418–426 (1999).
66. Han, C. H., Song, H., Kang, Y. G., Kim, B. M. & Im, C. H. Hemodynamic responses in rat brain during transcranial direct current stimulation: a functional near-infrared spectroscopy study. *Biomedical optics express*.**5**, 1812–1821 (2014).
67. Miller, S. & Mitra, K. NIRS-based cerebrovascular regulation assessment: exercise and cerebrovascular reactivity. *Neurophotonics*.**4**, 041503 (2017).
68. Hahn, G. H., Heiring, C., Pryds, O. & Greisen, G. Applicability of near-infrared spectroscopy to measure cerebral autoregulation noninvasively in neonates: a validation study in piglets. *Pediatric research*.**70**, 166–170 (2011).
69. Hong, K. S. & Yaqub, M. A. Application of functional near-infrared spectroscopy in the healthcare industry: A review. *Journal of Innovative Optical Health Sciences*.**12**, 1930012 (2019).
70. McKendrick, R., Parasuraman, R. & Ayaz, H. Wearable functional near infrared spectroscopy (fNIRS) and transcranial direct current stimulation (tDCS): expanding vistas for neurocognitive augmentation. *Frontiers in systems neuroscience*.**9**, 27 (2015).
71. Zhao, Z., Nelson, A. R., Betsholtz, C. & Zlokovic, B. V. Establishment and dysfunction of the blood-brain barrier. *Cell*.**163**, 1064–1078 (2015).
72. Brunoni, A. R. *et al.* Clinical research with transcranial direct current stimulation (tDCS): challenges and future directions. *Brain stimulation*.**5**, 175–195 (2012).
73. Antal, A. *et al.* Low intensity transcranial electric stimulation: safety, ethical, legal regulatory and application guidelines. *Clin. Neurophysiol*.**128**, 1774–1809 (2017).
74. de Roeper, I., Bale, G., Cooper, R. J. & Tachtsidis, I. in *Oxygen Transport to Tissue XXXIX* 141–147(Springer, 2017).
75. Merzagora, A. C. *et al.* Prefrontal hemodynamic changes produced by anodal direct current stimulation. *Neuroimage*.**49**, 2304–2310 (2010).
76. Yaqub, M. A., Woo, S. W. & Hong, K. S. Effects of HD-tDCS on resting-state functional connectivity in the prefrontal cortex: an fNIRS study. *Complexity* 2018 (2018).
77. Tachtsidis, I. & Scholkmann, F. False positives and false negatives in functional near-infrared spectroscopy: issues, challenges, and the way forward. *Neurophotonics*.**3**, 031405 (2016).
78. Zhang, Y., Brooks, D. H., Franceschini, M. A. & Boas, D. A. Eigenvector-based spatial filtering for reduction of physiological interference in diffuse optical imaging. *Journal of biomedical optics*.**10**,

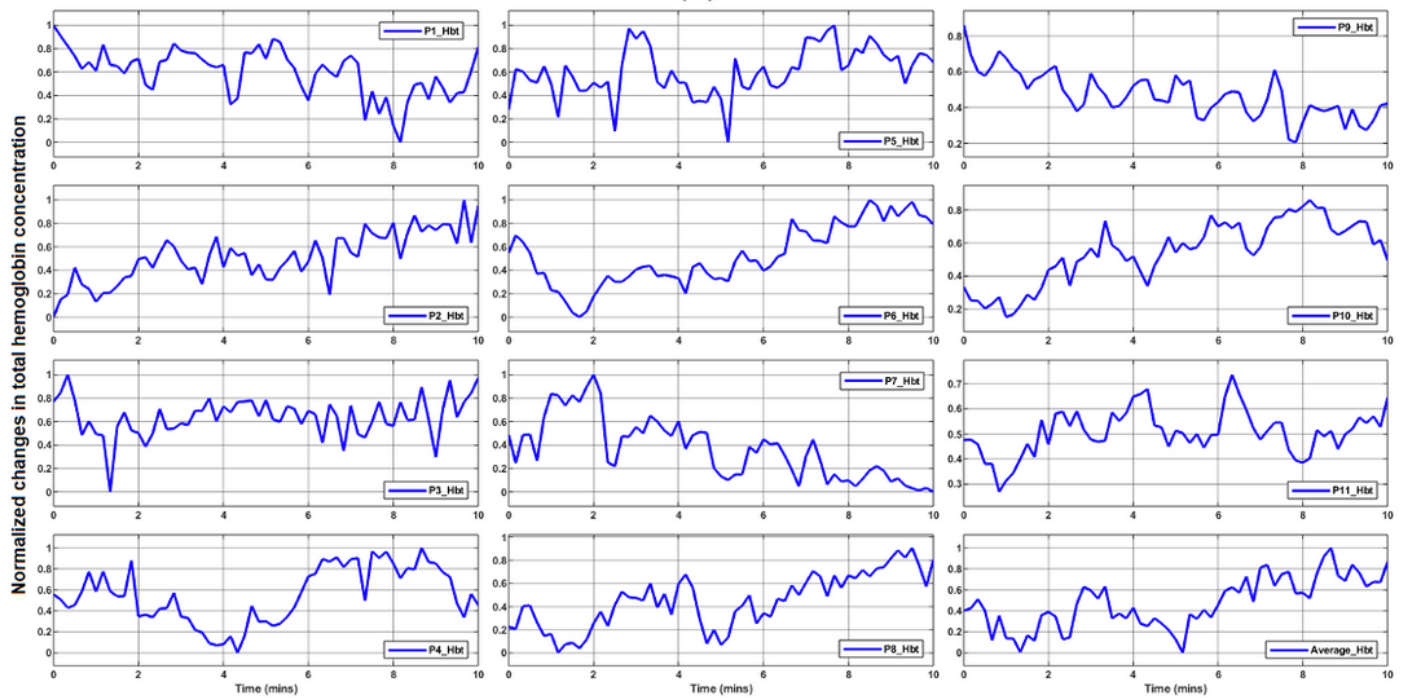
- 011014 (2005).
79. Nikulin, V. V. *et al.* Monochromatic Ultra-Slow (~ 0.1 Hz) Oscillations in the human electroencephalogram and their relation to hemodynamics. *Neuroimage*.**97**, 71–80 (2014).
 80. Pfurtscheller, G., Daly, I., Bauernfeind, G. & Müller-Putz, G. R. Coupling between intrinsic prefrontal HbO₂ and central EEG beta power oscillations in the resting brain. *PloS one*.**7**, e43640 (2012).
 81. Dormanns, K., Brown, R. & David, T. The role of nitric oxide in neurovascular coupling. *Journal of theoretical biology*.**394**, 1–17 (2016).
 82. Kenny, A., Plank, M. J. & David, T. The role of astrocytic calcium and TRPV4 channels in neurovascular coupling. *Journal of computational neuroscience*.**44**, 97–114 (2018).
 83. Mathias, E. J., Kenny, A., Plank, M. J. & David, T. Integrated models of neurovascular coupling and BOLD signals: Responses for varying neural activations. *NeuroImage*.**174**, 69–86 (2018).
 84. Chander, B. S. & Chakravarthy, V. S. A computational model of neuro-glio-vascular loop interactions. *PloS one***7** (2012).
 85. Witthoft, A., Filosa, J. A. & Karniadakis, G. E. Potassium buffering in the neurovascular unit: models and sensitivity analysis. *Biophysical journal*.**105**, 2046–2054 (2013).
 86. Chang, J. C. *et al.* A mathematical model of the metabolic and perfusion effects on cortical spreading depression. *PLoS One***8** (2013).
 87. Dormanns, K., van Disseldorp, E., Brown, R. & David, T. Neurovascular coupling and the influence of luminal agonists via the endothelium. *Journal of theoretical biology*.**364**, 49–70 (2015).
 88. Chhabria, K. & Chakravarthy, V. S. Low-dimensional models of “neuro-glio-vascular unit” for describing neural dynamics under normal and energy-starved conditions. *Frontiers in neurology*.**7**, 24 (2016).
 89. Blanchard, S. *et al.* A new computational model for neuro-glio-vascular coupling: astrocyte activation can explain cerebral blood flow nonlinear response to interictal events. *PloS one***11** (2016).
 90. Mathias, E., Plank, M. & David, T. A model of neurovascular coupling and the BOLD response: PART I. *Computer methods in biomechanics and biomedical engineering*.**20**, 508–518 (2017).
 91. Sten, S., Elinder, F., Cedersund, G. & Engström, M. A quantitative analysis of cell-specific contributions and the role of anesthetics to the neurovascular coupling. *NeuroImage*, 116827(2020).
 92. Amzica, F., Massimini, M. & Manfredi, A. Spatial buffering during slow and paroxysmal sleep oscillations in cortical networks of glial cells in vivo. *Journal of Neuroscience*.**22**, 1042–1053 (2002).
 93. Ruohonen, J. & Karhu, J. tDCS possibly stimulates glial cells. *Clinical neurophysiology*.**123**, 2006–2009 (2012).
 94. Huang, R., Peng, L. & Hertz, L. Effects of a low-voltage static electric field on energy metabolism in astrocytes. *Bioelectromagnetics: Journal of the Bioelectromagnetics Society, The Society for Physical Regulation in Biology and Medicine, The European Bioelectromagnetics Association*.**18**, 77–80 (1997).

95. Gellner, A. K., Reis, J. & Fritsch, B. Glia: a neglected player in non-invasive direct current brain stimulation. *Frontiers in cellular neuroscience*.**10**, 188 (2016).
96. Monai, H. *et al.* Calcium imaging reveals glial involvement in transcranial direct current stimulation-induced plasticity in mouse brain. *Nature communications*.**7**, 11100 (2016).
97. Kofuji, P. & Connors, N. C. Molecular substrates of potassium spatial buffering in glial cells. *Molecular neurobiology*.**28**, 195–208 (2003).
98. Trivedi, D. P., Hallock, K. J. & Bergethon, P. R. Electric fields caused by blood flow modulate vascular endothelial electrophysiology and nitric oxide production. *Bioelectromagnetics*.**34**, 22–30 (2013).
99. Zhao, Z. *et al.* Directing migration of endothelial progenitor cells with applied DC electric fields. *Stem cell research*.**8**, 38–48 (2012).
100. Molaee-Ardekani, B. *et al.* Effects of transcranial Direct Current Stimulation (tDCS) on cortical activity: a computational modeling study. *Brain stimulation*.**6**, 25–39 (2013).
101. Cedersund, G. Conclusions via unique predictions obtained despite unidentifiability–new definitions and a general method. *The FEBS journal*.**279**, 3513–3527 (2012).
102. Nitsche, M. A. *et al.* Transcranial direct current stimulation: state of the art 2008. *Brain stimulation*.**1**, 206–223 (2008).
103. Filosa, J. A. *et al.* Local potassium signaling couples neuronal activity to vasodilation in the brain. *Nature neuroscience*.**9**, 1397–1403 (2006).
104. Knot, H., Zimmermann, P. & Nelson, M. Extracellular K (+)-induced hyperpolarizations and dilatations of rat coronary and cerebral arteries involve inward rectifier K (+) channels. *The Journal of physiology*.**492**, 419–430 (1996).
105. McCarron, J. G. & Halpern, W. Potassium dilates rat cerebral arteries by two independent mechanisms. *American Journal of Physiology-Heart and Circulatory Physiology*.**259**, H902–H908 (1990).
106. Kenny, A., Zakkaroff, C., Plank, M. J. & David, T. Massively parallel simulations of neurovascular coupling with extracellular diffusion. *Journal of computational science*.**24**, 116–124 (2018).
107. Friston, K. J., Mechelli, A., Turner, R. & Price, C. J. Nonlinear responses in fMRI: the Balloon model, Volterra kernels, and other hemodynamics. *NeuroImage*.**12**, 466–477 (2000).
108. Roche-Labarbe, N. *et al.* Noninvasive optical measures of CBV, StO₂, CBF index, and rCMRO₂ in human premature neonates' brains in the first six weeks of life. *Human brain mapping*.**31**, 341–352 (2010).
109. Pavlov, G., Shi, D. & Maydeu-Olivares, A. Chi-square difference tests for comparing nested models: An evaluation with non-normal data. *Structural Equation Modeling: A Multidisciplinary Journal*.**27**, 908–917 (2020).

Figures



(A)



(B)

Figure 1

Normalized time course of changes in the total hemoglobin concentration (averaged over four fNIRS channels around 4x1 HD-tDCS anode) from the stimulated (A) and the non-stimulated (B) contralateral sensorimotor area of eleven healthy participants (P1_Hbt to P11_Hbt) as well as the average time course (Average_Hbt) during anodal HD-tDCS (2mA current for 10 minutes, with ramp-up period of 30 seconds)

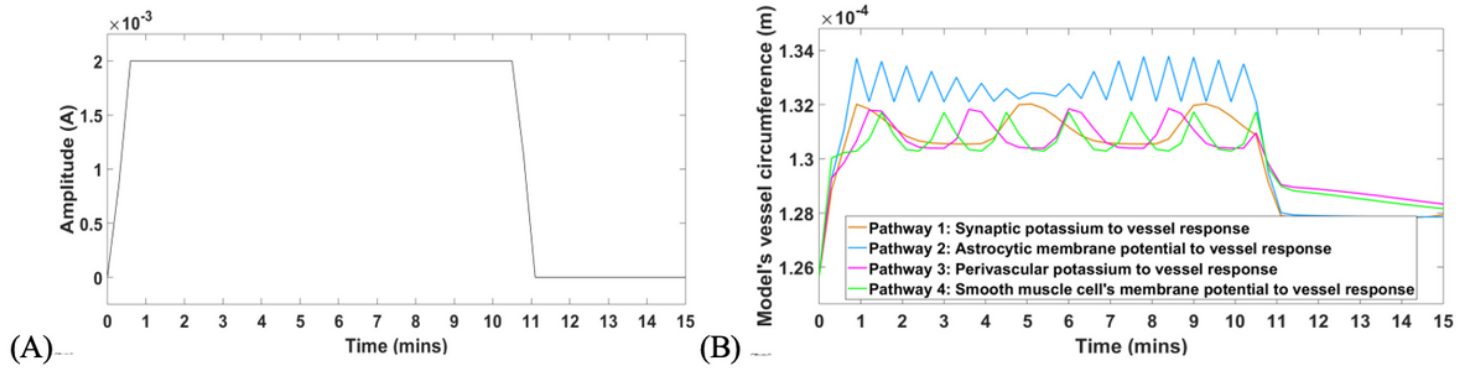


Figure 2

Physiologically detailed neurovascular coupling model showing the input HD-tDCS current (A) and output vessel circumference response for the four simulated pathways (B). Pathway 1: tDCS current density modulating vessel response through synaptic potassium pathway, Pathway 2: tDCS current density modulating vessel response through the astrocytic pathway, Pathway 3: tDCS current density modulating vessel response through perivascular potassium pathway, and Pathway 4: tDCS current density modulating vessel response through voltage-gated ion current channels on smooth muscle cells pathway. As shown in 2(B), the NVC pathways generated low-frequency oscillations in the frequency range of 0.05 – 0.2 Hz in the time course of the vessel response.

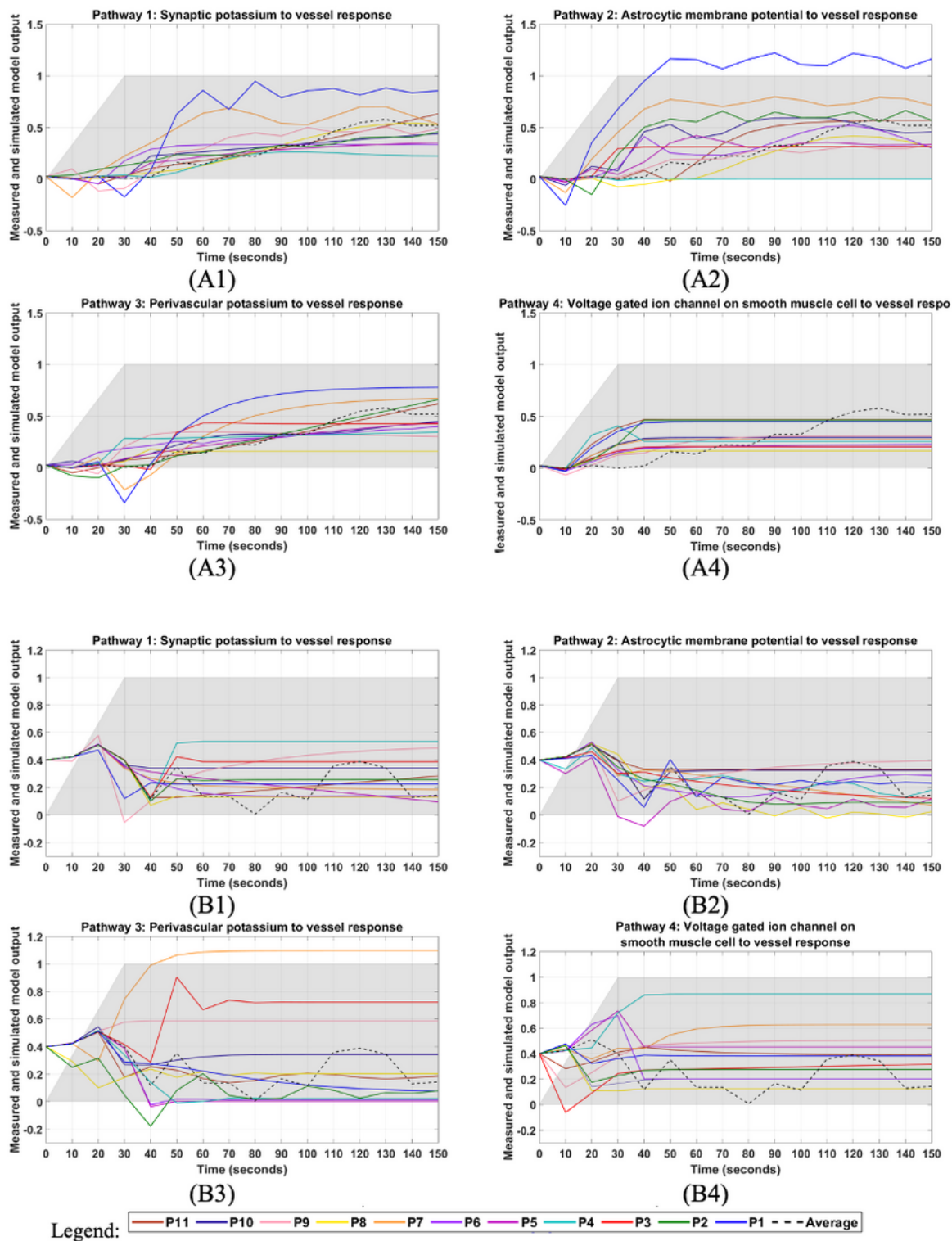


Figure 3

Simulated grey-box linear model output for the four pathways fitted individually to each of the 11 participants' fNIRS-tHb data during HD-tDCS (shaded grey). The average fNIRS-tHb response across all participants is also shown with a dashed line. Plots (A1) – (A4) show the four pathways fitted to the HD-tDCS stimulated sensorimotor data, while the plots (B1) – (B4) shows the four pathways fitted to the HD-tDCS non-stimulated contralateral sensorimotor data. Pathway 1: tDCS current density modulating vessel

(circumference) response through synaptic potassium pathway, Pathway 2: tDCS current density modulating vessel (circumference) response through the astrocytic pathway, Pathway 3: tDCS current density modulating vessel (circumference) response through perivascular potassium pathway, and Pathway 4: tDCS current density modulating vessel (circumference) response through voltage-gated ion current channels on the smooth muscle cells pathway.

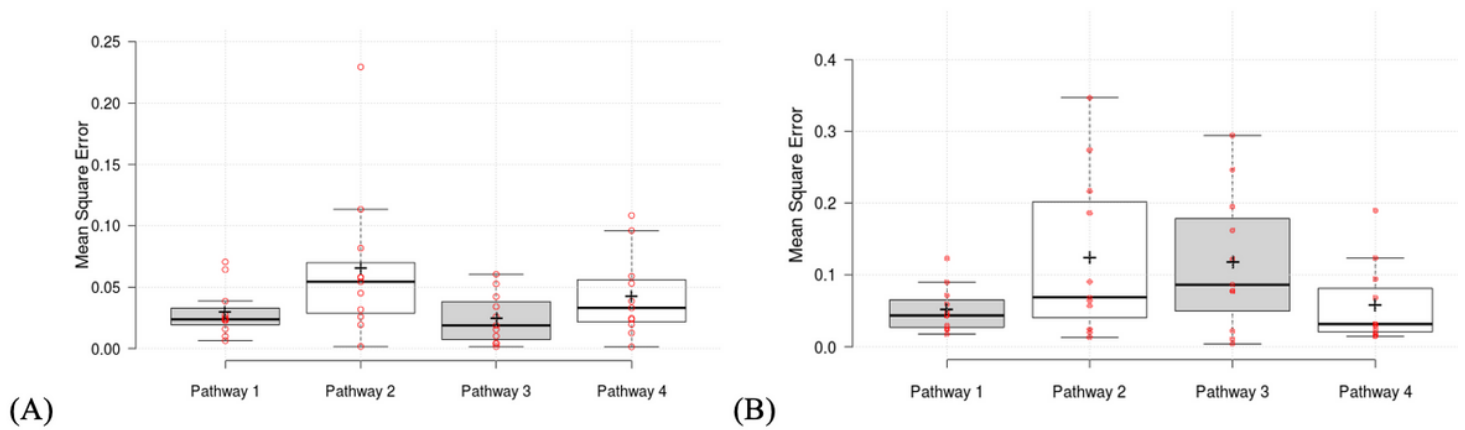
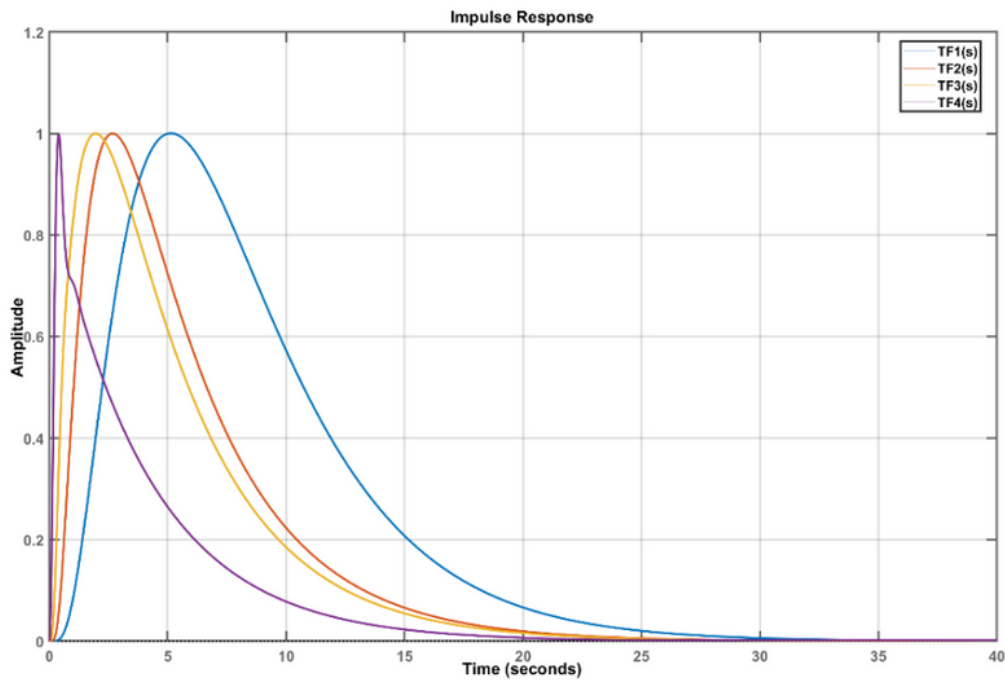
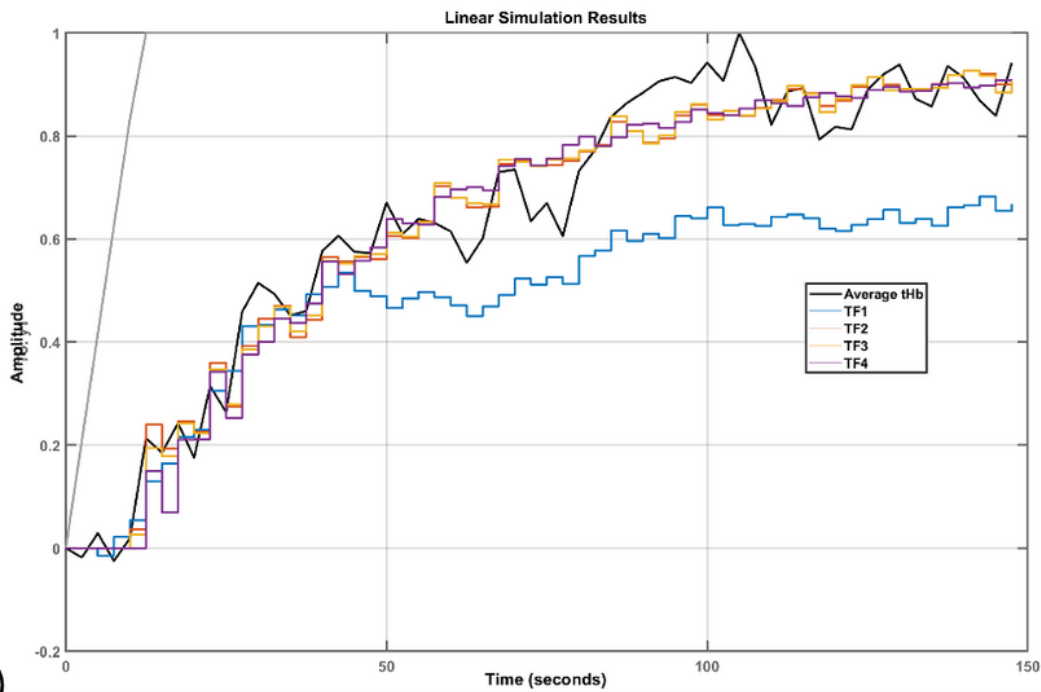


Figure 4

Boxplot of the mean square error (MSE) across 11 participants using the initial 150sec of fNIRS-tHb data from stimulated (A) and non-stimulated (B) sensorimotor area for the four model pathways. The central line mark indicates the median, and the bottom and top edges of the box indicate the 25th and 75th percentiles, respectively. The whiskers extended to the most extreme data points not considered outliers, and the outliers are plotted outside the box, and '+' symbol represents the mean value. Pathway 1: tDCS modulating vessel response through synaptic potassium pathway, Pathway 2: tDCS modulating vessel response through the astrocytic pathway, Pathway 3: tDCS modulating vessel response through perivascular potassium pathway, and Pathway 4: tDCS modulating vessel response through the SMC pathway.



(A)



(B)

Figure 5

(A) Normalized impulse response function of the minimal realization transfer function (see Table 2) for the four pathways (TF1(s): vessel response through synaptic potassium pathway, TF2(s): vessel response through the astrocytic pathway, TF3(s): vessel response through perivascular potassium pathway, and TF4(s): vessel response through smooth muscle cell pathway) of the reduced dimension grey-box linear model for the neurovascular unit compartment model – see Figure 9. (B) Linear model simulation of the

minimal realization transfer functions (TF1-TF4) of the four pathways fitted(all free parameters)to the normalized averaged (across participants) tHb time series.

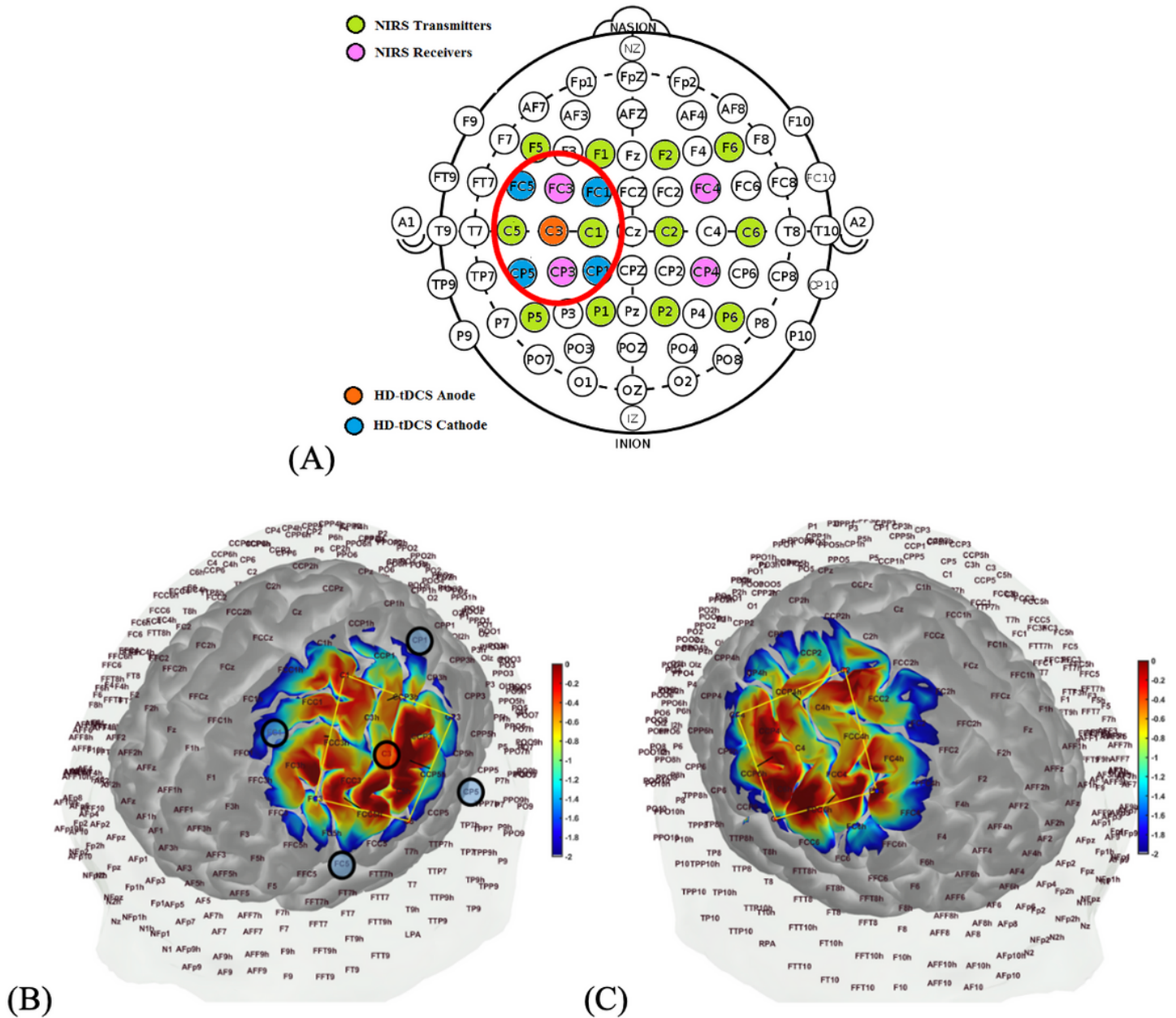


Figure 6

(A) HD-tDCS-fNIRS montage on a 10/10 EEG system. The fNIRS time series data from the transmitter-receiver optode combinations in the vicinity of 4x1 HD-tDCS electrodes (C5-CP3, C1-CP3, C5-FC3, and C1-FC3) as well as contralateral non-stimulated hemisphere (C2-FC4, C2-CP4, C6-FC4, and C6-CP4) were used for the grey-box modeling. (B) Measurement sensitivity of the fNIRS channels at the grey matter on the left hemisphere along with the HD-tDCS electrodes in the AtlasViewer open source package (<https://github.com/BUNPC/AtlasViewer>). (C) Measurement sensitivity of the fNIRS channels at the grey matter on the right hemisphere in the AtlasViewer open source package (<https://github.com/BUNPC/AtlasViewer>).

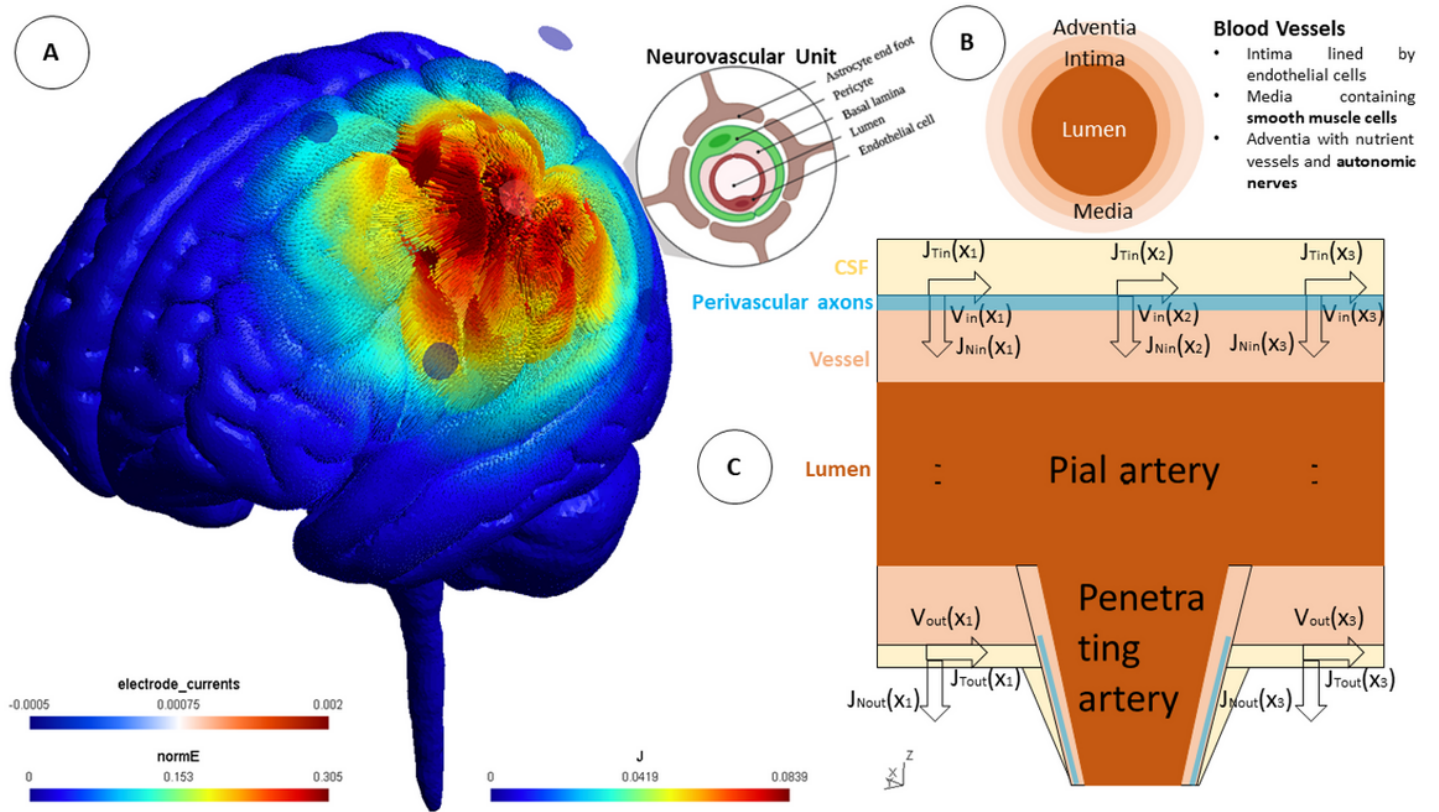


Figure 7

(A) Electric field strength (in V/m) along with the current density vector (in A/m²) computed at the gray matter surface due to 2 mA anodal HD-tDCS (4 x 1 configuration) over left sensorimotor cortex using finite element modeling in the SimNIBS open source package (<https://simnibs.github.io/simnibs/build/html/index.html>). (B) Blood vessels are composed of endothelial cells (in the intima layer), smooth muscle cells (in the medial layer), and extracellular matrix (containing the perivascular nerves), where the electric field can affect the smooth muscle cells and the perivascular nerves. (C) Perivascular nerves on the surface of pial vessels, on the surface of the brain are particularly susceptible to tangential surface current (J_{Tin}) due to the current spread in the highly conductive (mean 1.69 S/m) cerebrospinal fluid (CSF) boundary compared to grey matter (mean 0.60 S/m), blood (mean 0.58 S/m), and vessel wall (0.46 S/m). Spatial change in the J_{Tin} , e.g., along pial artery (X_1 , X_2 , X_3), can lead to the activating function that is proportional to the second spatial derivative of the extracellular potentials (V_{in} , V_{out}) along the axon.

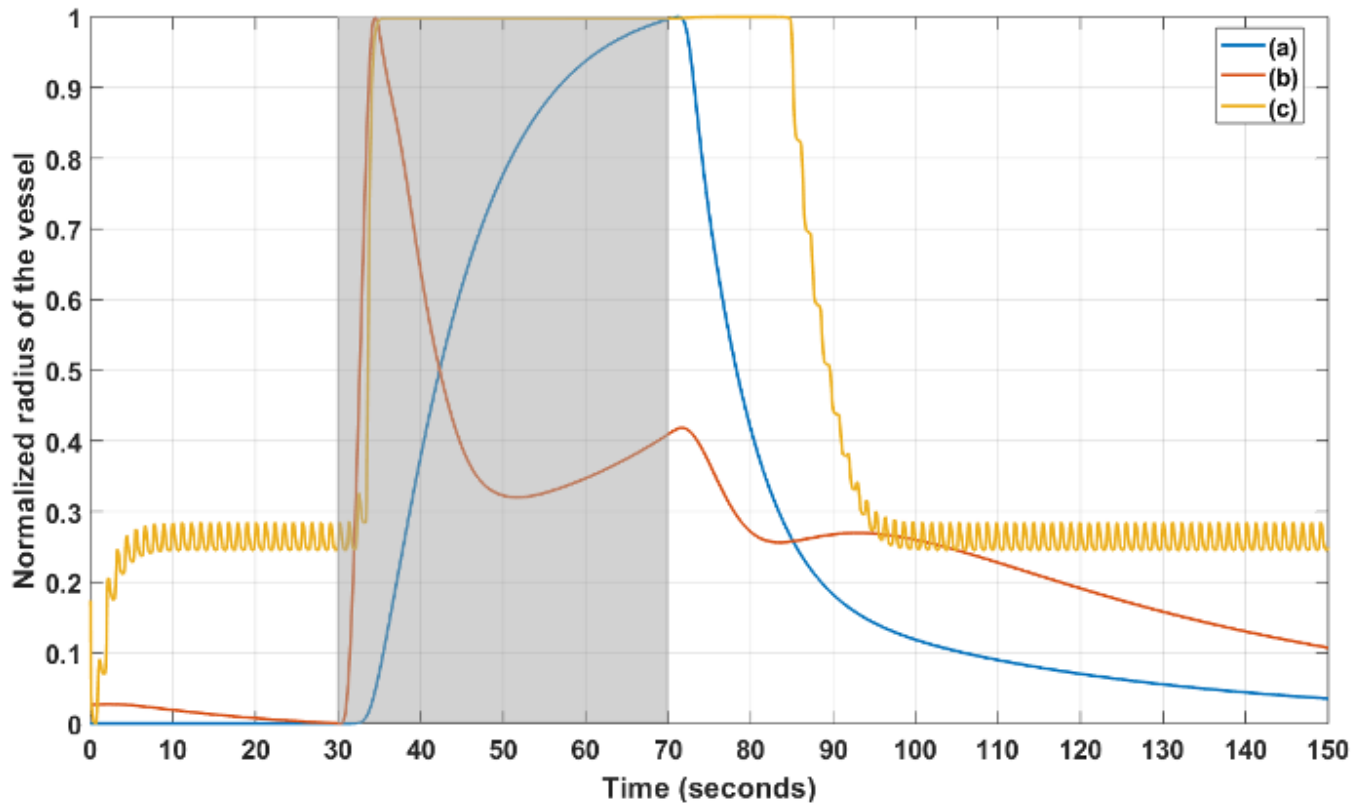
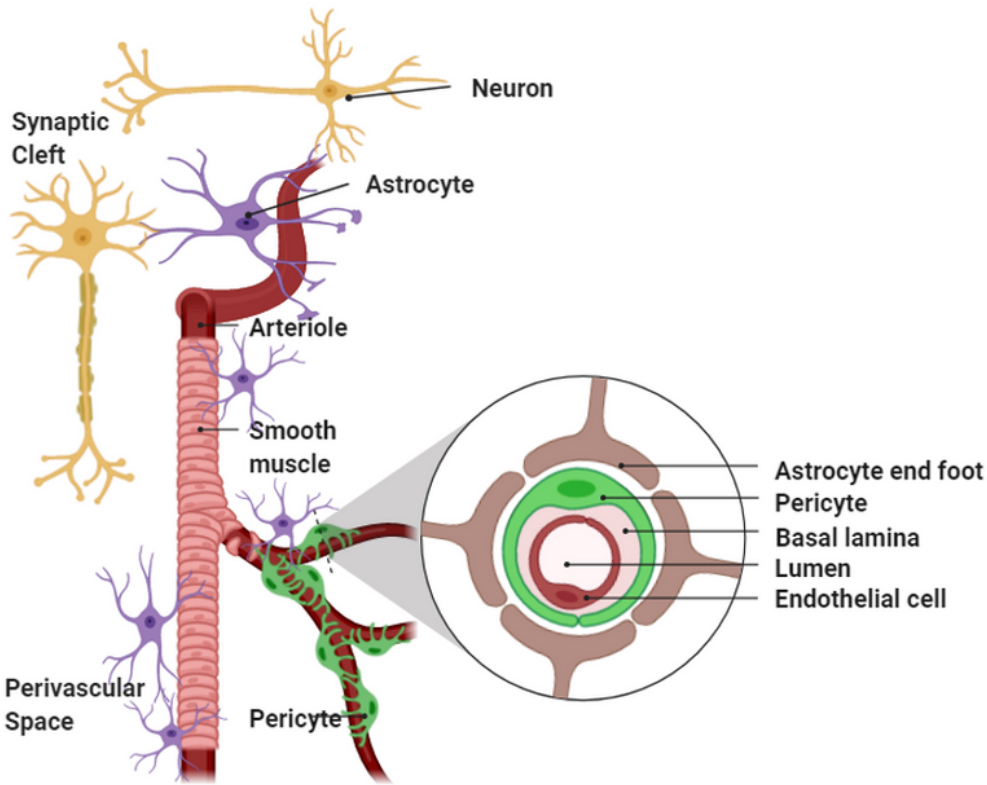
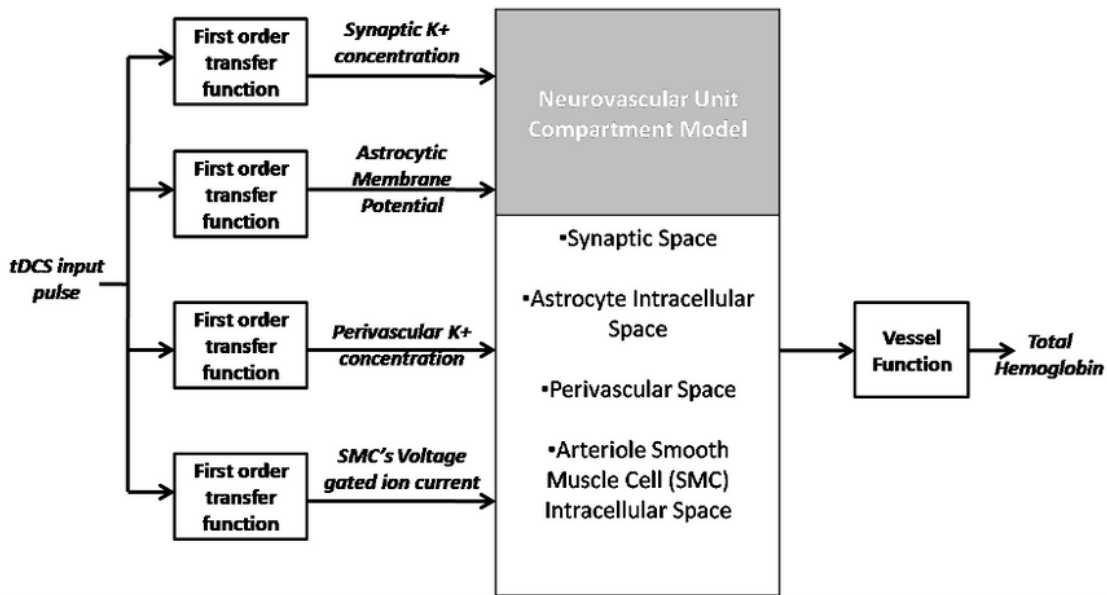


Figure 8

Normalized vessel radius changed from the detailed neurovascular unit models during neuronal stimulation (30 to 70 sec) shown by the shaded region. The period from 0 to 30 sec shows numerical transients where the model (c) settles to a non-zero vessel radius from zero initial condition. Model (c) also captured the after-effect of the neuronal stimulation on the normalized vessel radius. Three relevant physiological models simulation from Table 3: Model (a) Kenny et al., 2018, Model (b) Mathias et al., 2018, and Model (c) Witthoft and Karniadakis, 2012.



(A)



B)

Figure 9

(A) Anatomical representation using BioRender(<https://biorender.com/>) of the components of neurovascular unit that can be affected by tDCS current density in the neurovascular brain tissue. (B) Schematic representation of the four pathways for tDCS current density effects on vessel volume function (vessel circumference) for hypothesis testing using total hemoglobin concentration changes (proportional to blood volume). The four simulated pathways are, Pathway 1: tDCS current density (input

pulse) via first-order transfer function modulate vessel volume response (output) through synaptic potassium (K⁺), Pathway 2: tDCS current density (input pulse) via first-order transfer function modulate vessel volume response (output) through the astrocytic membrane, Pathway 3: tDCS current density (input pulse) via first-order transfer function modulate vessel volume response (output) through perivascular potassium (K⁺), and Pathway 4: tDCS current density (input pulse) via first-order transfer function modulate vessel volume response (output) through voltage-gated ion current channels on the smooth muscle cell (SMC).

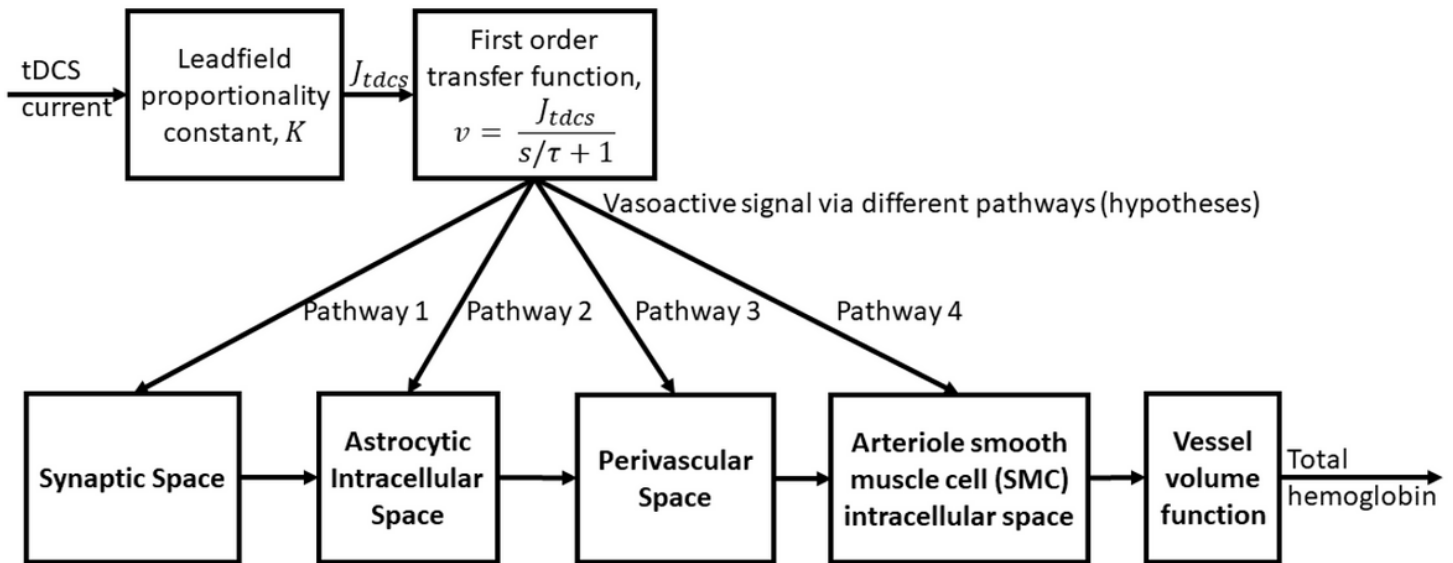


Figure 10

Block diagram of the four pathways for hypothesis testing

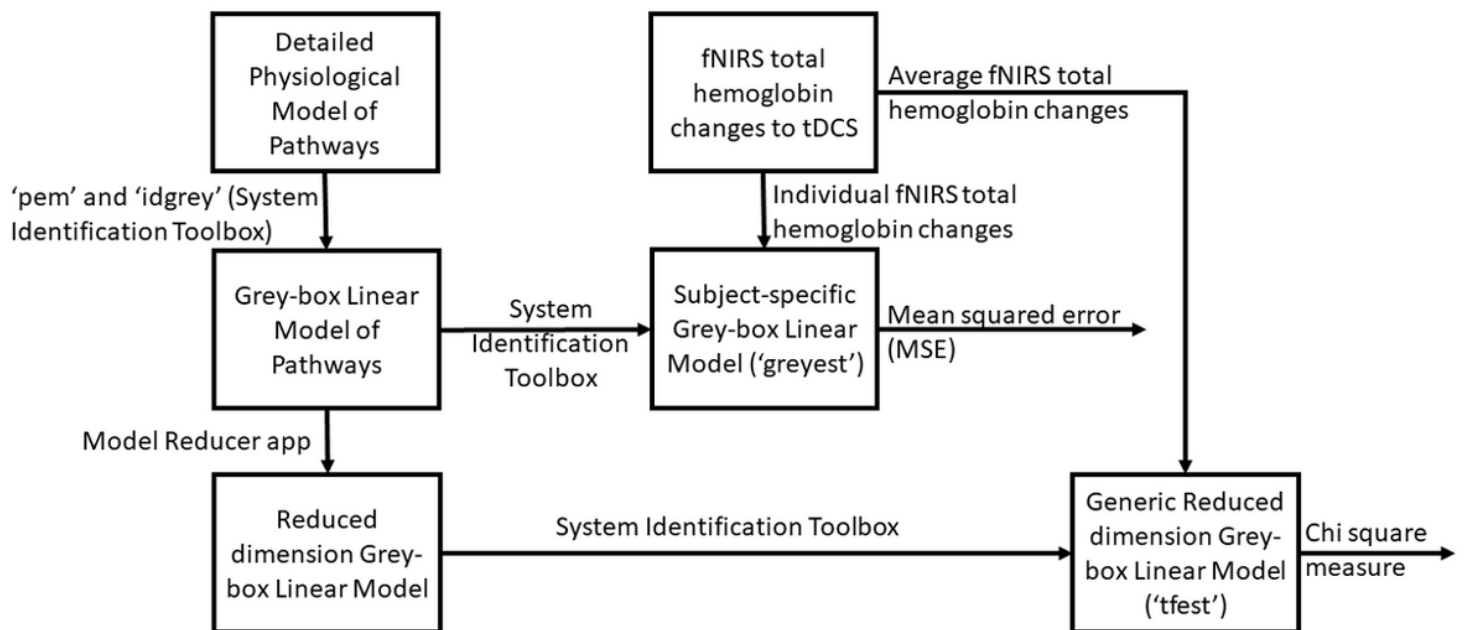


Figure 11

Supplementary Files

This is a list of supplementary files associated with this preprint. Click to download.

- [SupplementaryMaterials02082021.pdf](#)